UNIVERSIDADE
BEIRA INTERIOR

Piezoresistive Sandwich Structures: Assessing the viability of additive manufacturing and real-time monitoring for aerospace applications

(versão corrigida após defesa)

João Carlos Silva Moura

Dissertação para obtenção do Grau de Mestre em
Engenharia Aeronáutica
(mestrado integrado)

Orientador: Prof. Doutor Abílio Manuel Pereira da Silva
Co-orientador: Doutor João Pedro Nunes Pereira
Co-orientador: Mestre Martim Lima de Aguiar

junho de 2025

Declaração de Integridade

Eu, João Carlos Silva Moura, que abaixo assino, estudante com o número de inscrição a37630 do Mestrado Integrado em Engenharia Aeronáutica da Faculdade de Engenharia, declaro ter desenvolvido o presente trabalho e elaborado o presente texto em total consonância com o **Código de Integridades da Universidade da Beira Interior**.

Mais concretamente afirmo não ter incorrido em qualquer das variedades de Fraude Académica, e que aqui declaro conhecer, que em particular atendi à exigida referenciação de frases, extratos, imagens e outras formas de trabalho intelectual, e assumindo assim na íntegra as responsabilidades da autoria.

Universidade da Beira Interior, Covilhã 25 /06 /2025

Assinado por: **João Carlos Silva Moura**
Num. de Identificação: 14665481
Data: 2025.06.27 14:29:34+01'00'

CHAVE MÓVEL

To my friends and family, for their undying love and support; for trusting me when even I would not and giving me hope in times I found none.
It has been a privilege to live alongside you, and I am forever grateful to you all.

Agradecimentos

Antes de mais, gostaria de dar os meus agradecimentos ao Prof. Doutor Abílio Silva e ao Doutor João Pereira pelo seu incansável acompanhamento e apoio a todos os níveis ao longo desta dissertação, cuja realização se deve vastamente, e na generalidade, aos seus contributos.

Agradeço também ao Mestre Martim Aguiar a ajuda constante que foi dada, particularmente durante os processos de produção, sem a qual teria enfrentado grandes dificuldades no fabrico das estruturas.

Queria também estender os meus agradecimentos ao Departamento de Ciências Aeroespaciais, Departamento de Engenharia Eletromecânica, e C-MAST (Centro de Ciências e Tecnologias Mecânica e Aeroespacial), e ao Laboratório de Inovação e Tecnologias para a Sustentabilidade, da Universidade da Beira Interior, por garantirem as condições necessárias à realização desta dissertação, tanto pela disponibilização das instalações, equipamentos, consumíveis, e todos os materiais necessários, como por todo o apoio que foi dado durante o processo.

Por fim, aos meus amigos, colegas de curso, e família, um grande obrigado por todo o apoio, confiança e companhia ao longo desta dissertação.

Resumo

O uso de materiais compósitos, especialmente laminados e sanduíches, tem vindo a registar crescimentos significativos, tanto a nível qualitativo como quantitativo. Este facto deve-se às suas vantagens relativamente a opções tradicionais, nomeadamente no que se refere à resistência à fadiga, resistência e módulo específicos, e peso relativamente baixo. Estes fatores significam que o seu uso é altamente favorável em aplicações no setor dos transportes, nomeadamente na indústria aeroespacial. Em simultâneo, os avanços recentes em técnicas de fabrico e a mudança de paradigma para a integração de várias funções em materiais e componentes independentes indicam um potencial inegável para a melhoria dos processos de fabrico e multifuncionalidade destes compósitos.

Neste trabalho, foram desenvolvidas amostras tipo viga segundo os princípios de um compósito sanduíche, recorrendo ao fabrico tradicional de laminados usados nas peles, com a inclusão adicional de uma funcionalidade piezoresistiva, complementada por núcleos fabricados por técnicas de manufatura aditiva. Desta forma, promoveu-se a funcionalidade de monitorização elétrica, com o objetivo de demonstrar a viabilidade desta configuração de elementos num só componente. Procedeu-se também à criação de três tipos diferentes de núcleos para as sanduíches – de células hexagonais, auxéticas (reentrantes) e cúbicas – com o intuito de salientar as vantagens das geometrias possíveis apenas com recurso à manufatura aditiva.

Os resultados mostraram que a geometria cúbica se destaca por uma absorção de energia elevada: até 273 % superior à das outras geometrias; a auxética destaca-se por alcançar a maior deformação até à rutura: até 196 % superior à das outras opções; e a hexagonal apresenta uma degradação menor da tensão e do módulo de elasticidade com cada ciclo: até 26 % da degradação de ambos os valores nas outras geometrias. Além disso, todas as geometrias atingiram uma resposta piezoresistiva de elevada qualidade, demonstrando assim a sua viabilidade multifuncional.

Palavras-chave

Compósito Sanduíche; Manufatura Aditiva; Piezoresistividade; Resposta Eletromecânica; Monitorização em Tempo Real.

Abstract

The use of composite materials, especially laminates and sandwich materials, has been currently experiencing significant growth, both qualitatively and quantitatively; this fact is owed to their advantages over traditional options, namely with regards to their resistance to fatigue, stiffness and relatively low weight. These factors contribute to their preference in transport-related applications, namely in the aerospace industry. Simultaneously, recent advances in manufacturing techniques and a paradigm shift towards favouring materials and components that independently integrating multiple functions indicate an undeniable potential for the improvement of the manufacture and functionality of these same composites.

In this work, several beam-type samples were developed according to the principles of a sandwich-type composite, where the traditional fabrication for a laminate is complemented by additive manufacturing techniques and the additional inclusion of a piezoresistive component to promote an electrical monitoring capability, with the objective of demonstrating the viability of such a configuration of elements in a single component. Furthermore, three different types of cores were created for the sandwiches – with hexagonal, auxetic (re-entrant) and cubic cells – with the intention of emphasising the advantages and disadvantages of the various types of cells, namely those of a geometry only made possible by resorting to additive manufacturing.

These efforts highlighted the cubic geometry for its greater energy absorption: up to 273 % greater than other geometries; the highlight of the auxetic geometry was a superior strain at the yield point: up to 196 % further than the other options; and the highlight of the hexagonal was an inferior decline in stress and elastic modulus over cycles: up to 26 % of that observed for both values in other geometries. Furthermore, all geometries achieved a high-quality piezoresistive response, demonstrating multifunctionality.

Keywords

Additive Manufacturing; Sandwich Composite; Piezoresistivity; Electromechanical Response; Real-Time Monitoring.

Index

Figures

Tables

Acronyms

ABS	*Acrylonitrile Butadiene Styrene*
AM	*Additive manufacturing*
ASA	*Acrylonitrile Styrene Acrylate*
BAAM	*Big-Area Additive manufacturing*
CAD	*Computer-Aided Design*
CFR	*Continuous Fibre Reinforcement*
CFRP	*Carbon-Fibre Reinforced Polymer*
CLIP	*Continuous Liquid Interface Production*
DED	*Direct Energy Deposition*
DW	*Direct-Write*
EBF^3	*Electron-Beam FreeForm Fabrication*
FFF	*Fused Filament Fabrication*
FRP	*Fibre Reinforced Polymer*
GF	*Gauge Factor*
GFRP	*Glass-Fibre Reinforced Polymer*
LPF	*Laser Powder Forming*
MFC	*MultiFunctional Composites*
MFM	*MultiFunctional Materials*
MFS	*MultiFunctional Systems*
PA	*PolyAmide*
PC	*PolyCarbonate*
PEEK	*PolyEther Ether Ketone*
PET	*PolyEthylene Terephthalate*
PETG	*PolyEthylene Terephthalate Glycol-modified*
PLA	*Polylactic Acid*
PP	*PolyPhenylene*
PTFE	*PolyTetraFluoroEthylene*
REX	*Reactive Extrusion*
SLM	*Selective Laser Melting*
SLS	*Selective Laser Sintering*
SMM	*Shape Memory Material*
SSC	*Sandwich-Structured Composites*
TPU	*Thermoplastic PolyUrethane*
UV	*UltraViolet*

Symbols

b	mm	*Beam Width*
d	mm	*Beam Thickness*
E	MPa	*Elastic Modulus*
GF		*Gauge Factor*
l	mm	*Beam Length*
L	mm	*Support Span*
P	N	*Load*
R	Ω	*Electrical Resistance*
Ro	Ω	*Initial Electrical Resistance*
Rf	Ω	*Final Electrical Resistance*
$\frac{\Delta R}{R_0}$	%	*Relative Electrical Resistance*
ε	%	*Strain*
σ	MPa	*Stress*

1. Introduction

The aim of this initial chapter is to ease readers into the work by further contextualising the main themes herein and providing clear directions regarding the objectives of the work and the configuration of the document.

1.1 Motive

As part of the engineering domain, aerospace engineering is constantly driven by a natural and universal demand for improvement and innovation to further its goals. To this end, at the time of writing, MultiFunctional Systems (also known as MFSs) are undergoing investigation and conceptualisation as a promising alternative to – and, in some cases, an improvement over – more traditional single-function components, which have long been the norm. Besides improving efficiency via weight savings – a necessary concern in engineering, and even more so in aerospace applications – MFSs can consolidate different characteristics at a level of cooperative operation unseen in legacy systems. This allows for the production of components with new capabilities, which can themselves provide new, practical solutions to some commonplace problems.

To give one particularly relevant example, current-day aircraft logistics incorporate significant costs in terms of both time and resources to guarantee appropriate airworthiness of a given aircraft – in some cases maintenance, repair and overhaul represents up to 10% of airline operating costs [1].

As such, the development of solutions incorporating airframe health monitoring would streamline this process, thus saving time and resources (and potentially extend the life cycle of components), which would generally be desirable when available. If the structural components could be monitored seamlessly, it would be possible to carry out initial evaluations precluding the physical inspection of an aircraft by pre-emptively detecting potential points of failure, therefore minimising work hours, material expenditure and, especially, airframe downtime. MFSs can provide such a solution.

At the same time, composite materials are a significant part of the ongoing development of MultiFunctional Materials (MFMs) – namely those with an electrical-response capability, i.e. materials with the potential for real-time monitoring. Given that composite technologies are already ubiquitous in the aerospace and aeronautical industries (see Figure 1.1), there appears to be potential for the practical implementation of composites with both structural and monitoring capabilities in the near future.

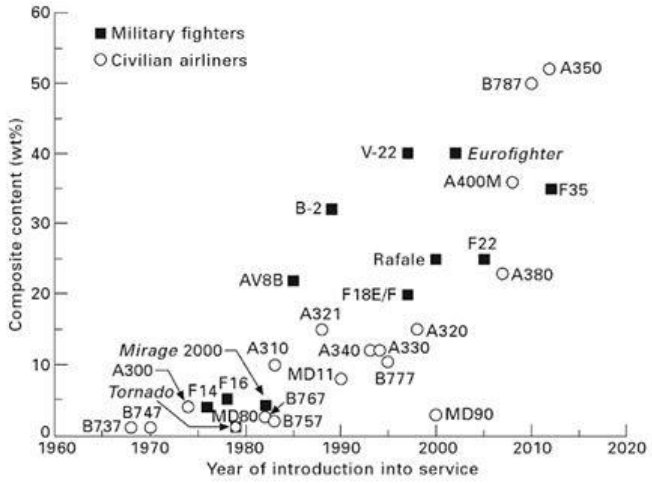

Figure 1.1 – Correlation between year of introduction and composite content for military and civilian airframes; reproduced from [2].

However, the traditional manufacturing techniques used for fabricating composites limit the scope of multifunctional components: in some cases, only a few different functionalities can be implemented, and the creation of more tightly integrated materials is highly impractical, if not impossible. These limitations present a sort of developmental "bottleneck" for MFSs, so it may be necessary to explore novel manufacturing methods to overcome these shortcomings; one possibility that holds potential is the production of composites using additive manufacturing (AM) techniques: multiple forms of AM have already proven capable of autonomously producing parts with 2 or more materials simultaneously. And with the advent of new technologies and feedstocks in the field of AM, such as continuous fibre reinforcement (CFR) machines, or microfibre filled thermoplastic filaments for Fused Filament Fabrication (FFF) machines, the potential for more practical solutions for the production of multifunctional composites (also known as MFCs) is steadily increasing.

Looking at these points, there seems to be at least a potential niche for the combination of AM technologies, composite materials and MFSs; this dissertation has been carried out with this in mind.

1.2 Objectives

The main objective of this dissertation is to explore new developments in additive manufacturing technologies, comparing different core topologies and incorporating an integrated piezoresistive component, resulting in multifunctional behaviour.

To this end, two follow-up objectives have been defined: firstly, to produce samples that successfully incorporate additive manufacturing techniques, a sandwich composite construction and a multifunctional capability via mechanical and electrical components; and secondly, to evaluate, characterise and compare three distinct types of the aforementioned samples, distinguished by changes in the cellular structure of their sandwich cores.

These objectives would then permit the characterisation of the mechanical and electrical response for these three core types through both destructive and cyclic testing, highlighting both the advantages and disadvantages of each type; furthermore, these tests would also allow the acquisition of the gauge factor, thereby validating the practical utility of including a piezoresistive capability in the samples and potentially providing another point of comparison between the samples.

1.3 Layout

The remainder of this document is divided into four further chapters describing: the state of the art, i.e. the current state of the subject matters (Chapter 2); the production and experimental procedures (Chapter 3); the selection and organisation of the data obtained (Chapter 4); and the conclusive analysis of the results, data and work as a whole (Chapter 5).

2. State of the Art

2.1 Sandwich-Structured Composites

Sandwich-Structured Composites (SSC) – so called for their construction – are a particular assembly for a composite part, especially notable for a high volume, in relation to traditional composites.

In essence, an SSC consists of at least two components – the core, and the skin – each contributing to complementary structural functions. Additionally, some SSCs may require a third component to bind the aforementioned skins and core together – usually referred to as an adhesive – depending on the materials and construction of both (Figure 2.1).

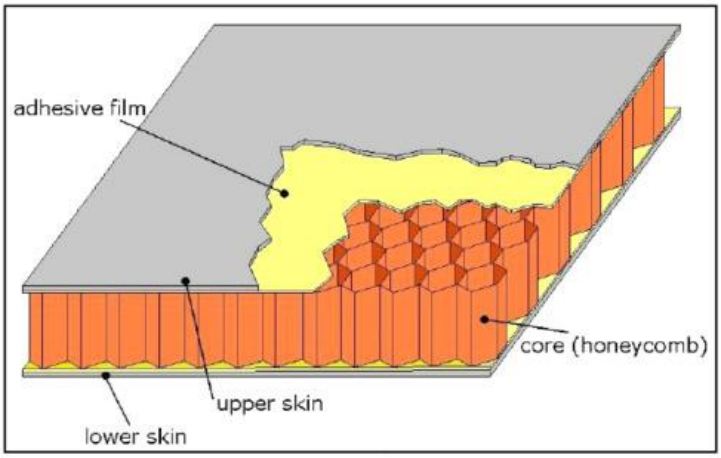

Figure 2.1- Illustration of a typical honeycomb-geometry SSC, reproduced from [3].

SSCs feature another number of perks, and significant advantages, over traditional composites, namely isolative properties, provided by their cores, and improved weight savings over laminates, at a sacrifice of overall volume. Evidently, these points – the latter especially – are highly relevant in an aerospace context.

2.1.1 SSC Elements, Types of Elements

As stated previously, an SSC is composed of a core, skins and, frequently, adhesive; however, each component may be one of various types and/or materials. In particular:

Core – homogenous and structured: aluminium, aramid, thermoset/thermoplastic polymers, foams, etc

Skins – Fibre-Reinforced Polymer(s) (FRP): Carbon-Fibre-Reinforced Polymer(s) (CFRP), Glass-Fibre-Reinforced Polymer(s) (GFRP), etc

Adhesives – epoxy, acrylic, silicone, etc

Furthermore, it should be noted that there exist cores combining characteristics of homogenous and structured cores – e.g. honeycomb cells with foam inserts within. However, these are rather niche and seldomly used. As such, these will not be discussed further.

Otherwise, adhesives are largely chosen as a function of the materials selected for the skins and core, and depending on production methods. Skins are likewise of minimal concern, in regards to structural design. An exception to this matter is the use of asymmetrical skins (Figure 2.2), which is rather exclusive to aerospace usage, particularly in military applications (e.g. helicopters, drones) [4].

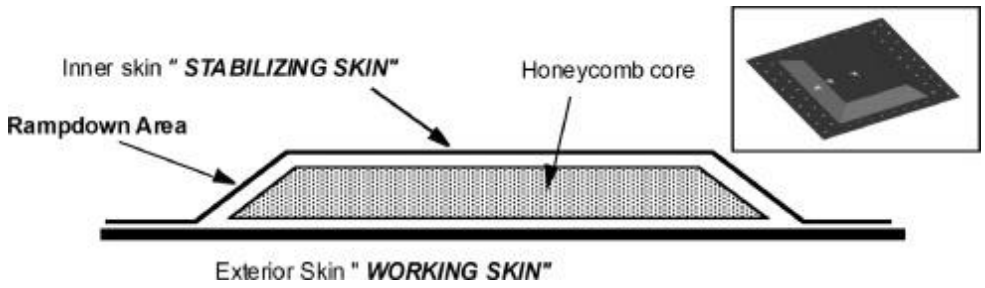

Figure 2.2 - Illustration of an asymmetrical honeycomb SSC, reproduced from [3].

2.1.2 Core Types and Geometries

The core of an SSC is a low-density, high-volume component – the core is the greatest contributor to the added volume of an SSC over its composite counterparts. In effect, the core separates the skins – and transfers and redistributes forces between said skins, while supporting shear, and bending stresses.

To this end, cores may be of naturally low-density materials, as a monolithic component – homogenous cores – or of other materials, arranged in particular geometries structurally, to achieve the same results – structured cores [5].

Homogenous Cores

Cores of this kind range from relatively primitive solutions, such as wood, to more advanced materials, such as purpose-built polymeric foams. Whichever the design, their simplicity does not sacrifice function; these cores also have the added benefit of increased contact surface with the skins compared to structured cores, and some may also function as insulators [2].

Structured Cores

As the name suggests, cores of this subset are comprised of structural solutions, and generally consist of a repeating geometric pattern.

In this role, honeycomb geometries are by far the more prevalent, particularly for aeronautical applications, such as Honeycomb cores are frequently fabricated from aramid and aluminium – the latter of which is especially common in aerospace applications.

However, other geometries are possible and available, chief among which are truss cores. Varied geometries have been produced (Figure 2.3), which perform differently than honeycomb cells, as detailed by Yuan et al.[6]; incorporating even perforated sheets, tubular elements, and rotating polygon structures [7].

Moreover, recent developments consisting of combining the more common honeycomb cells and new truss geometries, have resulted in hybrid cells showing great promise: according to Ingrole et al.[8], these cells offer great mechanical improvements over their honeycomb counterparts, and competitive performance compared to more advanced two-dimensional geometries, such as auxetic topologies for instance, which themselves can be integrated into the truss core concept [9]. Already, new auxetic metastructures are undergoing development with the aid of novel manufacturing methods [10].

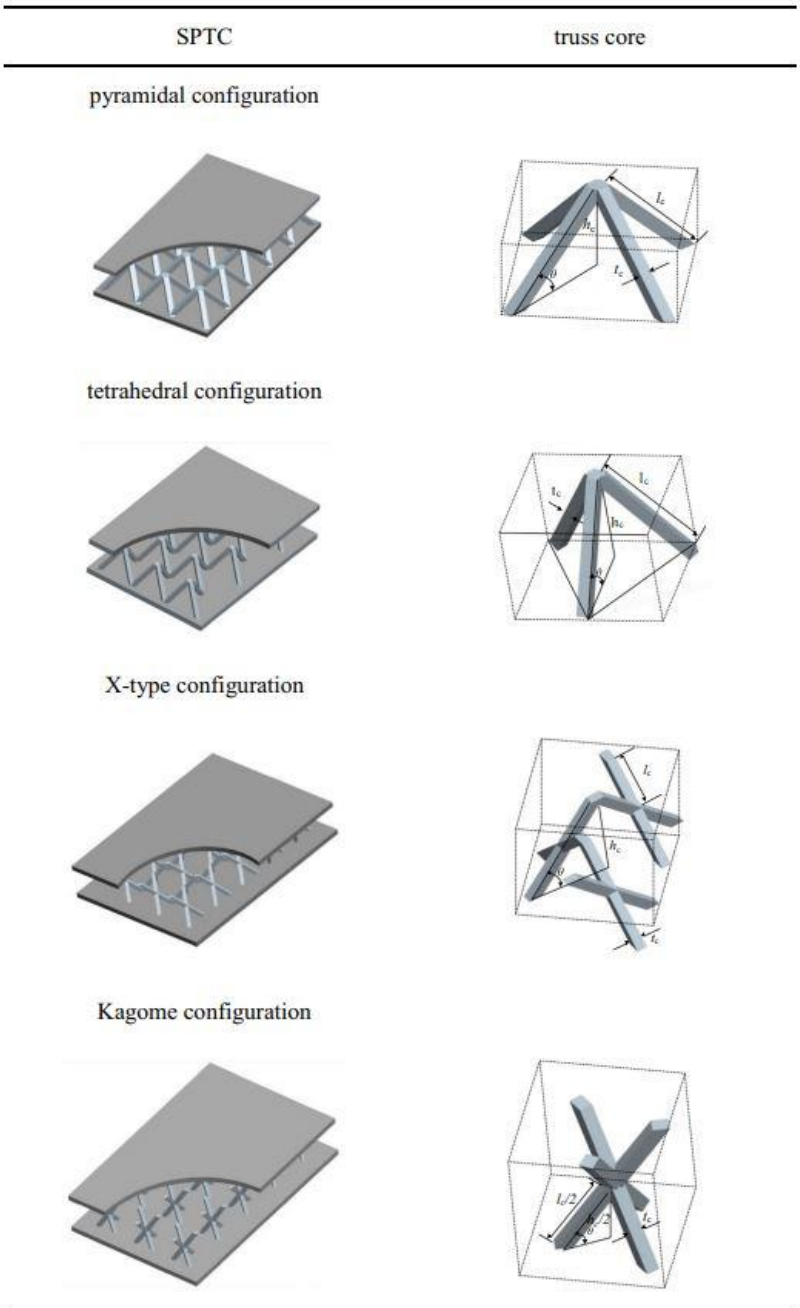

Figure 2.3- Different examples of truss configurations of different base geometries, reproduced from [6].

2.2 Additive Manufacturing

More commonly known as 3D-printing, Additive Manufacturing is a stark departure from traditional manufacturing methods; Additive Manufacturing (hereby referred to as AM) refers to a process that fabricates objects by depositing material based on digital 3D model data. This approach contrasts with subtractive manufacturing, where objects are created by removing material from a solid. In reality, while this statement's veracity has withstood the test of time so far, AM has branched out and significantly expanded from the traditional sense – that is, of a platform and a printing assembly, extruding a thermoplastic one layer at a time. In fact, there are types of AM systems that do not conform to any of the parameters of this description.

2.2.1 Types of AM

Since the materials, shapes, sizes, and generally the level of detail, bonding stress, and speed of production are related to the different approaches to AM, it is only natural that these are classified by matter of fabrication method, or hardware used. As such, AM types may be divided into the following groups, according to technique and from most to least pervasive:

Extrusion – self-explanatory, the part is built from a continuously-extruded filament;

Photopolymerization – the part is built within a tank of material in a liquid state, solidified via directed energy (i.e. lasers, heat);

Powder Bed Binding – the part is built in a tank of powdered material, fused using directed energy, much like the previous type;

Directed Energy Deposition – the part is built with the use of focused thermal energy, which both deposits and binds the material.

As noted above, extrusion-based AM is the more prominent, documented and relevant of these methods. Nevertheless, it is necessary to evaluate several manufacturing possibilities to determine the most objectively suitable type for a given scenario.

a. Extrusion

Fused Filament Fabrication.

Fused Filament Fabrication (FFF) represents the more widespread method of material extrusion AM and, indeed, of AM generally.

In FFF (Figure 2.4), the print is assembled in a layer-by-layer principle, with each layer being displaced along the Z-axis by a predetermined increment to "make way" for the next. Each layer is printed along the XY plane by a nozzle extruding and deposing material (i.e. molten polymer). The printing assembly contains, at a minimum, a heated nozzle to melt and extrude filament, rollers that supply material from a filament spool to the nozzle, and any components required for the operation of the aforementioned elements (e.g. fans to regulate the nozzle's temperature).

A typical print head generally consists of one, two or possibly more of these assemblies. Most FFF printers are single extruder in the interest of simplicity. Multiple extrusion configurations are also possible, allowing for the possibility of producing multi-material prints. This also allows for more

complex shapes where the first material is used for the printed part itself and a second material forms a support structure to hold the printed part. Support materials are frequently soluble or easily removable.

Feedstock materials used in FFF are often thermoplastics that do not demand complex printing settings such as PolyLactic Acid (PLA), Thermoplastic PolyUrethane (TPU) or PolyEthylene Terephthalate Glycol-modified (PETG) but heated printing chambers and the capability to achieve higher printing temperatures, allow for the extrusion of high-performance thermoplastics such as Acrylonitrile Butadiene Styrene (ABS), Acrylonitrile styrene acrylate (ASA), Polyamide (PA6, PA12), PolyCarbonate (PC), Polyethylene Terephthalate (PET), PolyPhenylene (PP), PolyEther Ether Ketone (PEEK), among others.

FFF can also operate with some microfibre-filled thermoplastics, namely those reinforced with carbon and glass microfibres: to this end, PolyAmide (PA), PETG, PLA and ABS are particularly common [11][12].

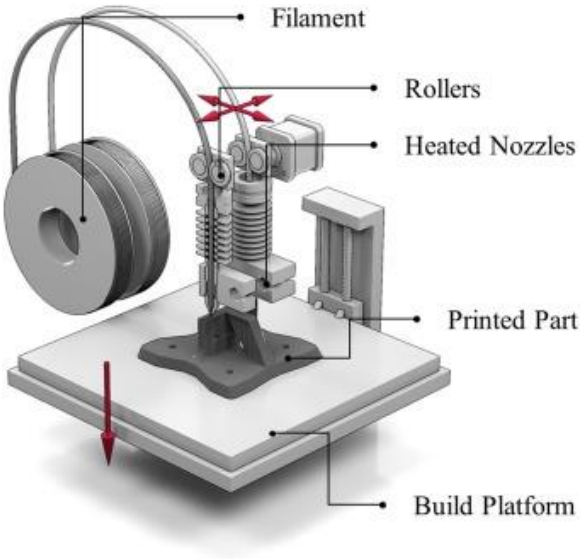

Figure 2.4- Illustration of a FFF printer, reproduced from [13].

Big-Area AM, Pellet-Based Fabrication.

Big-Area Additive Manufacturing (Figure 2.5), also known as BAAM, is a type of AM frequently used for fabricating large-scale components (e.g. industrial parts). Developed conjointly by Cincinnati Incorporated® and Oak Ridge National Laboratory, BAAM pioneered the concept of large-scale AM.

From a technical standpoint, the fundamental difference between BAAM and FFF – besides the size increase – is the feeding mechanism: BAAM dispenses with the filament spool, using pellets as feedstock instead. Once these polymeric pellets are melted within a heated barrel, they are pushed along the mechanism by a screw, into the nozzle. This results in both improved printing speed and costs over the more traditional means.

Moreover, this system excludes the need for an oven in the fabrication process, thus overcoming one of the greater design hurdles for larger part sizes: the difficulty in regulating temperatures over large AM builds.

In all other regards, BAAM is structurally similar to FFF.
Given how the polymeric pellets are formed into a filament during the fabrication process, BAAM may be classified as a type of FFF. However, there are sizeable differences between BAAM and the more typical FFF methods, which justify the differing classifications. Materials used in this system are usually either pure or carbon-reinforced polymers [14].

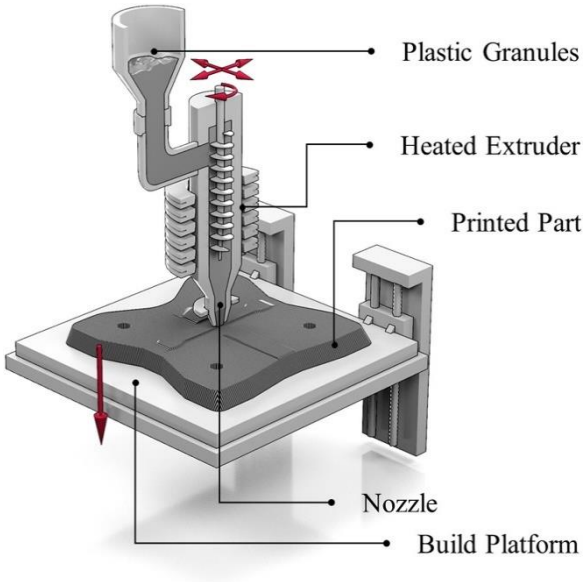

Figure 2.5- Illustration of a BAAM printer, reproduced from [13].

Direct-Write Fabrication, Reactive Extrusion.
Direct-Write (or DW) Fabrication and Reactive Extrusion (REX) consist of a similar mechanism to FFF, excepting the use of a slurry feedstock pumped through the nozzle. The most widely used materials in DW and RE are ceramics, conductive inks, or biomaterials (i.e. biopolymers for biomedical use, natural or synthetic).
The use of a slurry represents a particular problem for AM, since it lacks the consistency needed to retain shape as new layers are printed. DW and REX address this distinctly:
In DW, the material is cured concurrently with the printing process: to this end, the nozzle may be fitted with an ultraviolet (UV) light or a laser, curing the printed piece immediately.
In REX, two different materials are mixed as they pass the nozzle – a reactive polymeric resin, and a corresponding catalyst. The reaction therein results in an exothermal cure of the resin.
Additionally, some slurries might display enough viscosity to allow printing directly (this also depends on the size and shape of the print). However, generally speaking, these are still subjected to a curing process posteriorly.

b. Photopolymerization

Stereolithography.

Stereolithography makes use of a liquid feedstock, contained within a tank with a moving, translucent bottom piece. In this configuration, the printing component – a UV laser – is installed underneath the tank, which is used to polymerize the liquid resin through the translucent bottom. Upon successfully printing a layer, the tank's bottom piece descends by one increment, allowing the liquid contained within to flow and fully occupy the space between the translucent screen and the last printed layer.

CLIP, SGC.

Relatively to Stereolithography, Continuous Liquid Interface Production (CLIP) (Figure 2.6) makes use of a moving a fixed tub for the resin, illuminated by a UV light, and incorporates an ascending build platform. Instead of lowering the resin, the CLIP system raises the printed piece gradually.

The main design departure from traditional photopolymerization (i.e. stereolithography) is that the UV light allows the illumination of the part's XY cross-section entirely. In conjunction with a build platform moving at a constant pace, this enables the printing process to be truly continuous. The resulting increase in speed is claimed to be up to two orders of magnitude greater than conventional stereolithography.

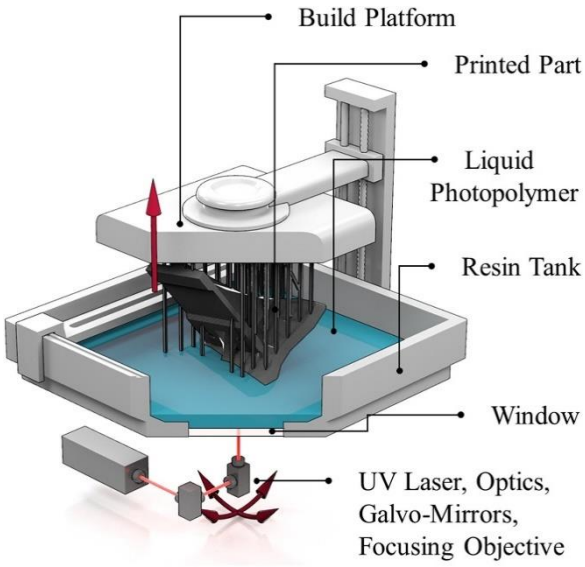

Figure 2.6- Illustration of a CLIP printer, reproduced from [13].

c. Powder Bed Binding

Selective Laser Sintering, Selective Laser Melting.

Both SLS (Figure 2.7) and SLM draw from the same powder bed concept, while differing in binding methods: those being sintering and melting, for SLS and SLM respectively. Both systems make use of a laser.

In both cases, it is possible to fabricate parts with very high mechanical properties: the powder feedstock is generally of a metal – namely aluminium, titanium, tool-grade steel, and nickel-based super alloys.

However, these have significant disadvantages – e.g. very high energy requirements, low technological maturity, and are highly dangerous if mishandled. Moreover, parts produced via SLS and SLM often display a porous, grainy surface, though this can be overcome with post-fabrication processes if needed. Even still, these are excellent for rapidly producing tools and for high-grade prototyping.

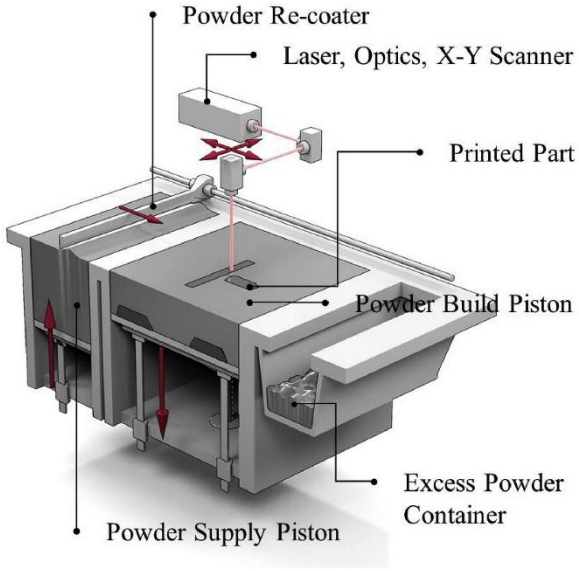

Figure 2.7 - Illustration of a SLS printer, reproduced from [13].

d. Directed Energy Deposition

Directed Energy Deposition (referred to as DED) is a type of AM that simultaneously inputs heat and material into the build platform. The heat is provided by a laser, electron-beam, or plasma arc – similarly to some methods previously discussed – and the feedstock is usually a powder, often fed by a stream of inert gas, or a wire. Metals – e.g. titanium, stainless steel, aluminium, and copper – are some of the most typically utilised materials.

In the case of the inert gas/powder mixture, it is possible to obtain a compositional gradient (i.e. a Functionally Graded Material) by using multiple nozzles fed with different powders. However, this method results in a relatively less favourable efficiency, as the gas does not contribute to the printed material. On the other hand, the wire-fed system represents a more traditional feeding approach.

It should also be noted that, if an electron beam is used for a heat source, a vacuum chamber is required. Electron-Beam FreeForm Fabrication (EBF3) and Laser Powder Forming (LPF) are two examples of possible configurations for DED – of an Electron-Beam / Wire Feedstock DED and a Laser / Powder DED, respectively.

2.3. Multifunctional Systems

As previously stated, multifunctional systems (MFS) are materials that fulfil two or more functions; to be more accurate, MFSs are characterised by a capacity to satisfy a multitude of functions of different fields – i.e. a material that contributes two structural functions to a system does not constitute an MFS. The fundamental principle of an MFS is the optimisation of a systems performance [15][16]. Note that this concept of multiplicity of functionality may also be applied to elements made up of any number of materials. In fact, there are also descriptors for MultiFunctional Materials (MFM) and Multi-Functional Composites (MFC). However, for the sake of simplicity, this terminology will be avoided whenever possible; instead, MFS will be used as an "umbrella term" for all terminology pertaining to multi-functionality – MFM/MFS/MFC – from this point onwards (Figure 2.1).

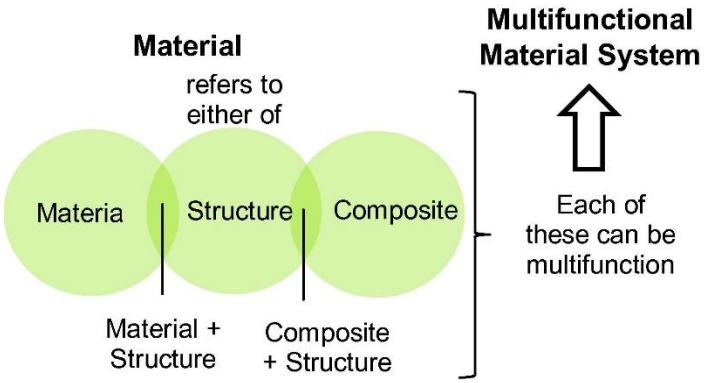

Figure 2.8 - Diagram for the primary nomenclature, reproduced from [15].

2.3.1. Scale and Scope

Differentiating MFSs along scales of, for instance, physical size, would be helpful for convenient identification. In their paper regarding MFSs, Ferreira et al.[15] suggest systems of physical scale, scope of autonomy, and degree of integration.

Proportions

Regarding size, MFSs may be defined by the smallest scale available that still includes one of the elements in full; naturally, this is mostly relevant for composites, justifying the mentality behind this scale, familiar to any kind of composite, regardless of number of functionalities. As such, while following the International Standard (SI) of measurement, MFSs may be divided as:

Picomaterials: 1-1000 picometre (pm)

Nanomaterials: 1-1000 nanometre (nm)

Micromaterials: 1-1000 micrometre (μm)

Mesomaterials: 1-1000 millimetre (mm)
as suggested again, by Ferreira et al.[15].
Note that an MFS may contain multiple scales, if comprised of several components, each of which potentially being of a different size scale.

Autonomy
As a product of the intended use of some MFSs – namely of the self-sensing or self-healing kind – these may achieve a level of self-sufficiency, to varying degrees.
Ferreira et al. [15] also suggest a six-category for multi-functional systems, based on their capabilities:
Passive: sensor-capable.
Sensory: sensor and actuator integration.
Active: sensory, with improved actuator capabilities.
Adaptive: sensory, with a great degree of control integration.
Intelligent: pairing of sensor, actuator, control, and processor functions.
Autonomous: intelligent system, coupled with power generation and/or storage, and increased degree of control.
Integration
For systems composed of multiple elements, there is the additional need for describing how well, or to what capacity, these elements interface with each other. In blending materials of different capabilities, a system can achieve multiple functions. These may also be used to characterise interface amongst multiple MFSs. Peter Matic suggests three categories [16]:
Type I: non-integrated, e.g. a structure incorporating a health-monitoring "skin".
Type II: partially integrated, e.g. a composite, with embedded elements functioning as antennas.
Type III: fully integrated, e.g. load-bearing polymer batteries.
Naturally, new categories may arise with further research and development, however for the moment and given the scope of this document, these three types should be sufficient.

2.3.2. Types of MFSs

MFSs may respond in a number of different ways to a great variety of stimulus, in theory. As such, these have hereby been categorised by type of stimulus – i.e. the MFS in question responds when affected by:
Thermal Energy: Thermochromic and thermoelectric, responding by changing colour and producing voltage respectively, and other thermal-responsive characteristics.
Mechanical Stress, Pressure: Piezoresistive and piezoelectric, producing voltage when under stress mechanically, and smart gels.
Magnetic Field: Magnetorheological, magnetostrictive and magnetocaloric for responses consisting of variation in shape, produced mechanical stress, and temperature differential, respectively.

Electrical Current: Changing shape or generating mechanical stress under voltage, through piezoelectric effect; generating heat under voltage, via thermoelectric effect; and electrochromic, which change colour when effected by electrical current.
Radiated Light: Photochromic and photomechanical, resulting in changes in colour and shape each.
Molecular Presence: Sensing the presence of certain molecules, particularly for gases.
pH Value: Responding to pH-value variations with changes to shape or colour.
However, given the lack of maturity of the subject matter, only a few types of MFS have seen concrete developments. Some of the more documented types are those using the piezoresistive effect, followed by the piezoelectric effect, and thermo- and magnetorheological materials.

a. Piezoresistive

The piezoresistive effect (also named electroresistive effect, interchangeably) denotes a change in electrical resistivity in a material, as a result of applied mechanical stress. Materials with this property are capable of health-monitoring functions, since the electrical resistivity can be measured at different loadings and then compared to reference values.
Piezoresistive materials generally consist of semiconductors – e.g. silicon, boron, certain carbon-based materials such as carbon nanotubes, even some natural polymers [17]. Additionally, these materials may be doped (i.e. have impurities added to them), as a means of further manipulating electrical and mechanical properties.
MFSs of this kind lack the functionality of piezoelectric-effect MFSs; for instance, they are incapable of functioning as actuators. However, piezoresistive-type MFSs are more easily produced and integrated, given the comparatively broad array of available materials, particularly in the form of composites – which is to say, type II MFSs – which may be created with as little as the introduction of one or more single-layer film(s) within [18]. One such example is the carbon films developed by Petersen et al.[17]. These dedicated sensors are reported to be highly sensitive and, as such, appropriate for addition to a given composite part.
Another means of achieving a type II piezoresistive MFS is to introduce a conductive component – e.g. carbon nanotubes – into a liquid solution, such as an uncured resin, prior to its integration into an FRP. In this configuration, electrical current may be conducted through the resin by the carbon nanotubes as long as they are present in a sufficiently high amount. The evolution of the electrical conductivity of an otherwise non-conductive doped composite in relation to the density of the conductive “doping” element is described by the principles of percolation theory. According to Santos et al. [19], percolation theory dictates that the electrical conductivity does not increase linearly with the addition of a conductive component, but in three distinct phases: initially the increase is lower until a percolation threshold is reached, at which point a composite achieves conductive behaviour; further increases beyond this point result in an accelerated increase in electrical conductivity, but eventually plateau as multiple, simultaneous conductive pathways begin to be established. These conductive processes occur both through direct contact of the carbon nanotubes and through separated nanotubes via the tunnelling effect, where «adjacent

conductive particles must be separated by small distances, typically on the order of 10^{-1} nm. This separation enables what is known as percolative conduction, where electrons can tunnel from one particle to another, facilitating the overall flow of electric current».
On the other hand, type III piezoresistive systems are also viable; it is possible to achieve an adequate piezoresistive performance, at a system-wide scale, by CFRPs. This process, as demonstrated by Yan et al.[20], may change not just piezoresistive properties, but also the corresponding model of the effect.
In essence, systems incorporating the piezoresistive effect aim to add health-monitoring capabilities to a given component, while minimising the impact to mechanical/structural performance.

b. Piezoelectric

MFSs of this category may be of both electrical current, and mechanical stress stimuli; either responding to mechanical stress with production of electric current, or responding to electrical current by changing shape, bending, expanding, and other mechanical responses. These different "directions" of action may also be referred to, respectively, as direct piezoelectric effect, and as inverse piezoelectric effect.
The piezoelectric effect is, generally, observable in particular crystalline materials – quartz being a chief example of one. In usage, these consist of single crystals (as the case previously stated), ceramics (named piezoceramics), and polymers (named piezopolymers). In the context of MFSs, the latter two types of materials classes see by most usage by far, given their ease of integration, which isolated crystals do not share.

Inverse Piezoelectric effect.
Inverse piezoelectric effect is most promising for the development of actuators – i.e. providing a system with the ability to expand, bend, or torque/twist on command. Most current day piezo actuators function as a component of Type I MFS, and contribute considerable bulk for the systems they integrate, while not contributing to the load-bearing capacity of the MFS [16].
At this time, type II MFC piezo actuators are under development, as a further technological step. In this role, piezoceramics are considered a better option than fibre-reinforced piezopolymers, due to the latter's fragility and inferior actuating forces – though piezopolymers may still see use wherever a system's geometry prevents the use of piezoceramics, due to their brittleness [15][18]. The inclusion of this kind of MFS in a wing's surface has been implemented by Li et al.[21] with the express purpose of improving aerodynamic performance.

Direct Piezoelectric effect.
Direct piezoelectric effect, in contrast, allows the production of sensors, for health monitoring purposes. Most of the available, sensing-capable MFS are Type I, and are often used as an add-on for non-multifunctional structures, particularly in civil engineering [15]. Logically, as the

aforementioned case is a largely independent, “smart layer” (Figure 2.2) (i.e. a thin film with passive sensor capabilities) addition, it is largely non-relevant.

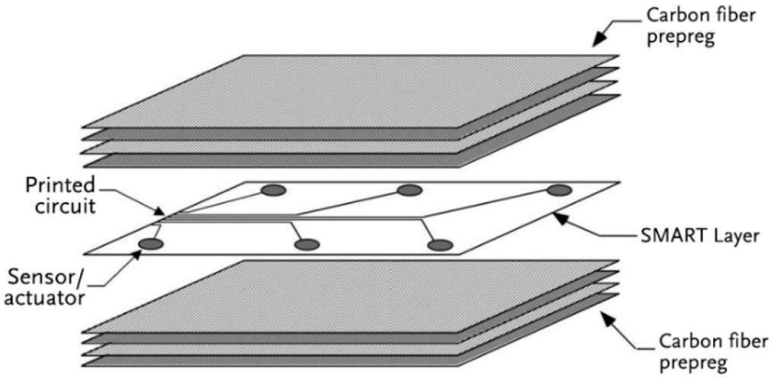

Figure 2.9- Illustration of SMART layer wedged within a laminated composite, reproduced from [15].

Generally, piezopolymers have been favoured for these applications, although piezoceramics are also in use [18].
However, when incorporated in MFCs, both of the Type I and Type II kind, these become highly relevant for aerospace applications, given the pervasiveness of composites in this sector/field and the added benefit of incorporating health-monitoring sensors internally, as internal damage is both common and difficult to assess [15].
Indeed, such MFCs have already been produced and tested, such as the one created by Lin, and Chang, which constitutes a carbon fibre composite housing a single sensory layer within [22].

c. Both

In addition to these roles, piezoelectric effect MFS may also be used for energy harvesting (e.g. damping vibrations, while converting them into usable energy simultaneously). Although MFS may be purpose-built to generate energy, systems harnessing both direct and inverse piezoelectric effect for actuation and sensing can also harvest energy to a degree. One such example would be a wing spar, developed by Wang [23], capable of multiple non-structural functions such as energy generation and health monitoring.

d. Thermorheological and Magnetorheological

Thermo-reactive and magneto-reactive MFS are both frequently used as a means of manipulating a systems’ shape. The most common application of this effect would be in the form of shape memory materials (SMM). In this function, these materials can return to an original form when exposed to sufficient thermal energy – e.g. heating a metal above austenite transformation temperature, leading to a change in shape at a macro scale – or when put under magnetic influence.
These effects are more immediately appreciable when using metals, namely metallic alloys. For instance, a prototype wing was developed by Sofla et al. [24] with integrated SMM, allowing the wing to morph via heating the corresponding components.

There are other applications for SSM, such as noise reduction, as seen in the variable geometry chevron (Figure 2.3), developed by Boeing, added to a jet engines trailing edge for the forementioned reason [25].

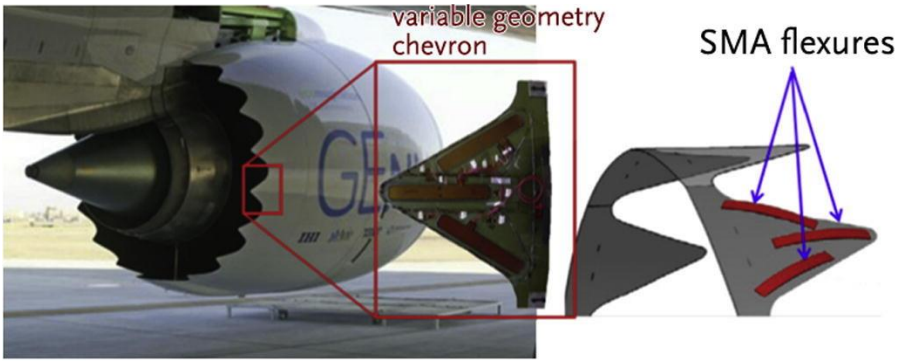

Figure 2.10 - Boeing-made Variable Geometry Chevron, reproduced from [15].

SMM are also closely related to self-healing MFS, as they expedite the process of bridging cracks and fractures, bringing a component closer to original shape even when damaged. As demonstrated by Huang et al.[26], a thermorheological SMM (Figure 2.4) can be used to compress another broken element back into shape, prior to further repairs, in a Type I MFS.

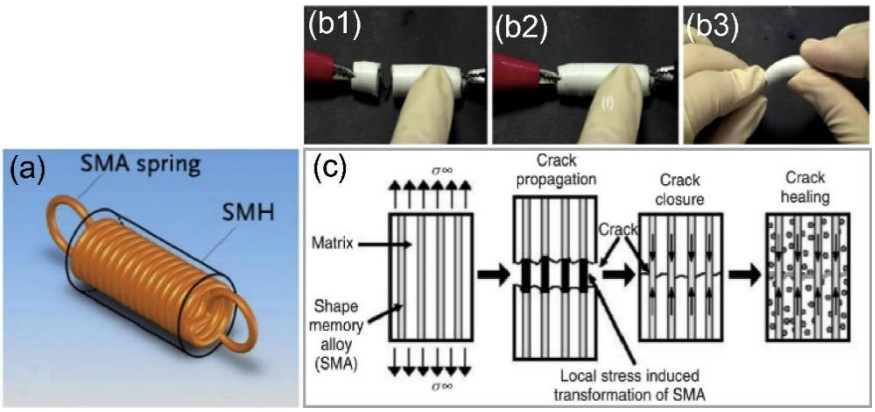

Figure 2.11 - Self-Healing device, reproduced from [15].

In addition to metal alloys, there are also polymer-based SMMs. These are more particular to the context of transportation, especially in the aerospace sector, due to weight savings over the previous SMMs.

The usage of these is particularly noteworthy for the development of self-deployable structures; a self-deploying radio reflector has been created using such polymers, by Kelller et al.[27], resulting in greater simplicity and reduced mass over traditional methods.

3. Experimental Procedure

3.1 Materials and Manufacture

Now, with the list of potential usable materials finalised, it is possible to proceed with the material selection and fabrication.

3.1.1. Core

Firstly, the options for printing the core come down to FFF and CLIP fabrication, since other methods are either not practical for the subject matter – e.g. BAAM and pellet-based fabrication – or are not entirely attainable for this project – e.g. powder bed binding such as SLS. Of the first two options, FFF was favoured due to its relative ubiquity/availability and overall low production cost, as well as the ease of transport and handling of feedstock compared to CLIP (spools of filament for the former versus liquid resins for the latter) and especially its greater printing speed – all of which should make FFF more suitable for production in unconventional/less than ideal locations.

The choice of FFF for the core means that the options for core materials are somewhat limited, both in terms of type and mechanical properties. At the same time, there are other considerations such as ease of use – e.g. some materials may release toxins during printing. Considering all this, PETG was chosen as the core material as it was the mechanically better-performing option available while not requiring any special printer setup and handling – i.e. mechanically preferable to PLA but less challenging to work with/print than PC to give an example (see Table 3.1) (Figure 3.1).

Table 3.1 – Estimated/Typical properties and recommended printing settings for filaments by manufacturer eSun© [28].

	Density [g/cm³]	Tensile Stress [MPa]	Elongation at Break [%]	Flexural Stress [MPa]	Flexural Modulus [MPa]	Extruder Temperature [°C]	Printing Bed Temperature [°C]	Fan Speed [%]	Printing Speed [mm/s]
PLA	1.2	72	11.8	90	1915	210-230	45-60	100	40-100
ABS	1.04	43	22	66	1177	230-270	95-110	100	40-100
ASA	1	50	30	35	4300	240-270	90-110	0	40-100
PETG	1.27	52.2	83	58.1	1073	230-250	75-90	100	40-100
PC	1.12	54.88	150.24	63.41	1073	240-260	80-120	0	20-50

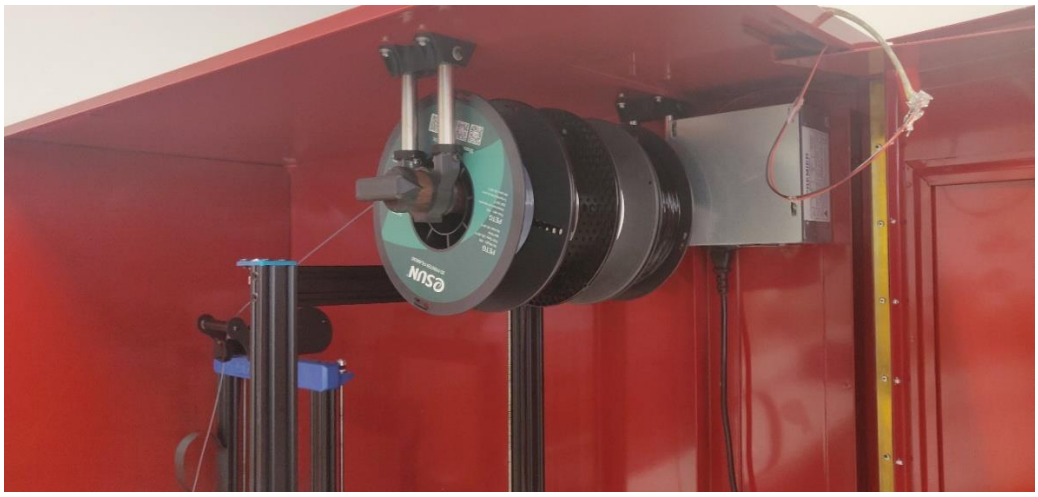

Fig 3.1 – Roll of PETG filament being fed to an FFF printer.

To this end, an eSun©-supplied spool of PETG was used, in conjunction with a Artillery3d© Genius printer. A translucent filament (which is, in fact, the natural colour for PETG filament) was selected, with hopes that it would allow for better visual analysis of the inner damage sustained by the cells during testing. With this, the fabrication of the core can begin. However, before the printing can begin per se, the 3D model of the cores is required. For this task, the chosen CAD software was SolidWorks©, due to user familiarity and preference, as well as ease of use (Figure 3.2).

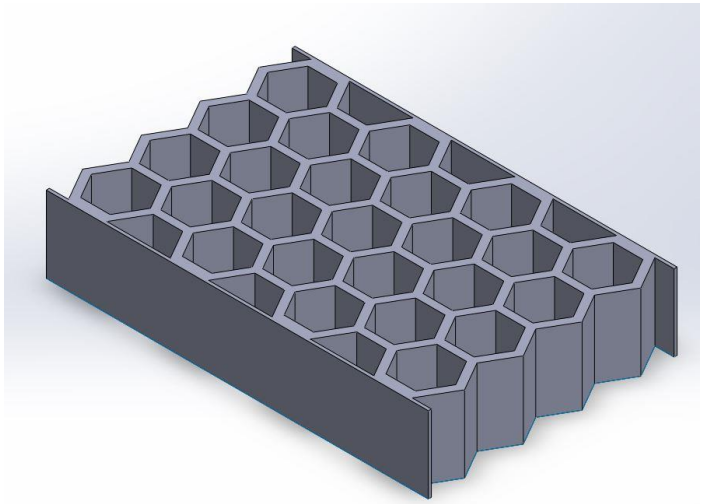
Figure 3.2 – Isometric view of a prototype core in SolidWorks©.

At this stage, the cores' dimensions were defined, and they were designed with external dimensions of an 80.0×23.4×10.0 mm, and an inner thickness of 1 mm for the cell walls. Additionally, since three cores were planned as previously detailed in section 1.2 – hexagonal, auxetic and cubic – the inner cells were dimensioned so that the cores would share a similar number of cells. The aim was to include twenty cells in each core to properly observe interactions between cells (this would become rather troublesome in the case of the cubic cells). Thin 0.4 mm thick skins had also been added directly to the cores to improve surface contact with the skins and

prevent poor adhesion and subsequent separation of the skins from the core. Hexagonal (Figure 3.3) and auxetic (Figure 3.4) cores were simply drawn two-dimensionally.

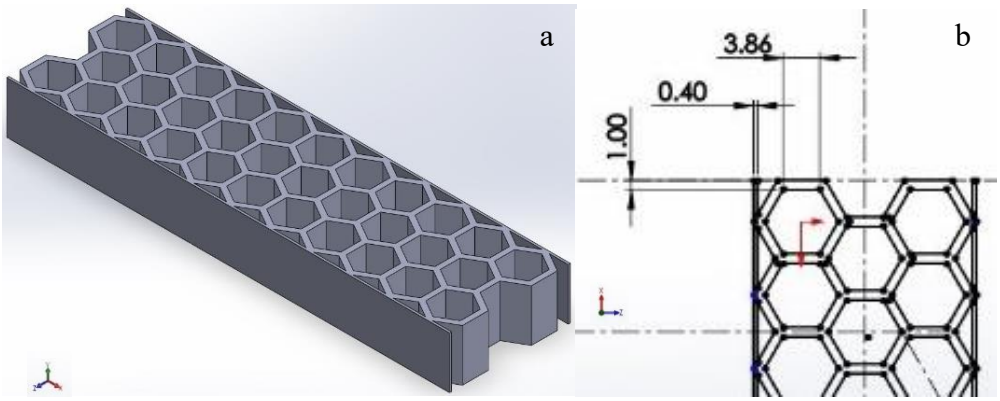

Figure 3.3 – Isometric view, a; and profile view, b, of a core with hexagonal geometry cells in SolidWorks©.

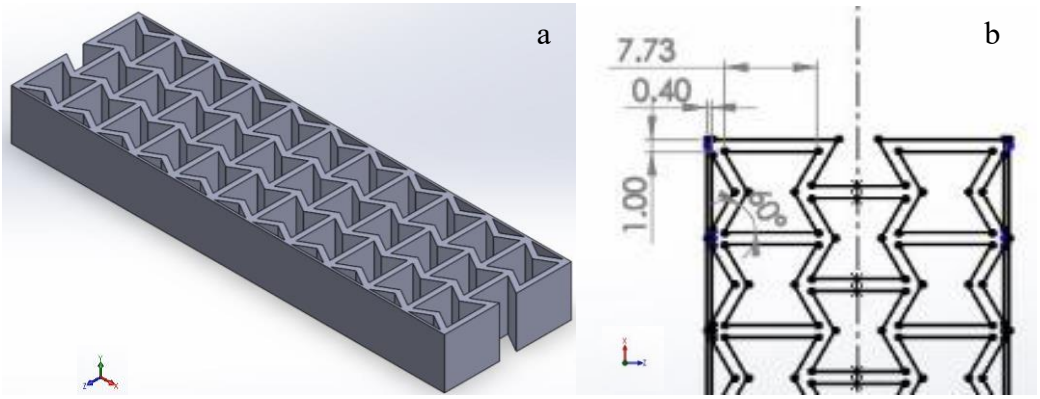

Figure 3.4 – Isometric view, a; and profile view, b, of a core with auxetic geometry cells in SolidWorks©.

When designing the core for the hexagonal and auxetic topologies, a single cell was first created as-is and was then sequentially repeated across the X-axis and Z-axis. The 0.4 mm skins were then added to the "top" and "bottom" of the profile (left and right in the two-dimensional profiles in Figure 3.3 and Figure 3.4). Once all the cells were fitted together, and both the cell and the external dimensions were correct, the profile was extruded to the desired thickness of 10 mm. However, the cubic cell topology is three-dimensional and therefore demanded a different approach (Figure 3.5).

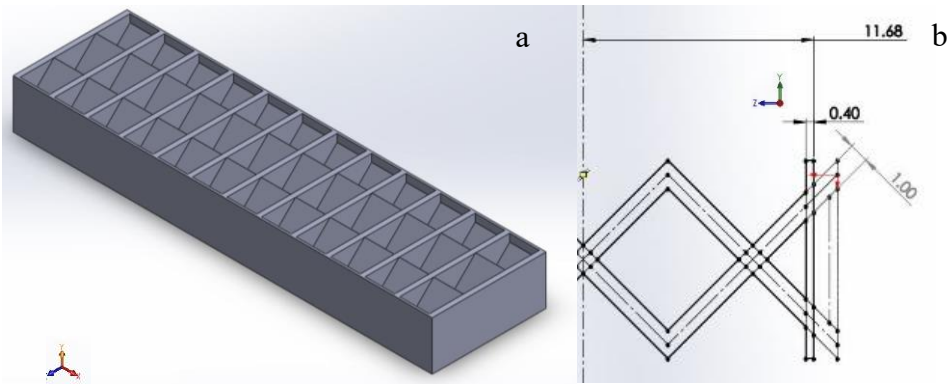

Figure 3.5 – Isometric view, a; and profile view, b, of a core with cubic geometry cells in SolidWorks©.

To ensure that the cells retain cubic proportions, and remain comparable to the previous cells, the cubes were rotated forty-five degrees about the Y-axis. This allows the cells to fit within the 10 mm thickness of the core, without reducing their size compared to other cells. Furthermore, this solves another issue with the cubic topology: due to the nature of FFF manufacture, a hollow cube facing the printing bed generally necessitates the inclusion of support structures, to prevent horizontal walls from falling as they are printed. With the cubic cells' edges facing the printing bed instead of their faces, the cells can be printed at a 45º degree angle, requiring no supports.
The slicing process begins once the cores are drawn – the software employed for this step was Ultimaker Cura© (Figure 3.6).

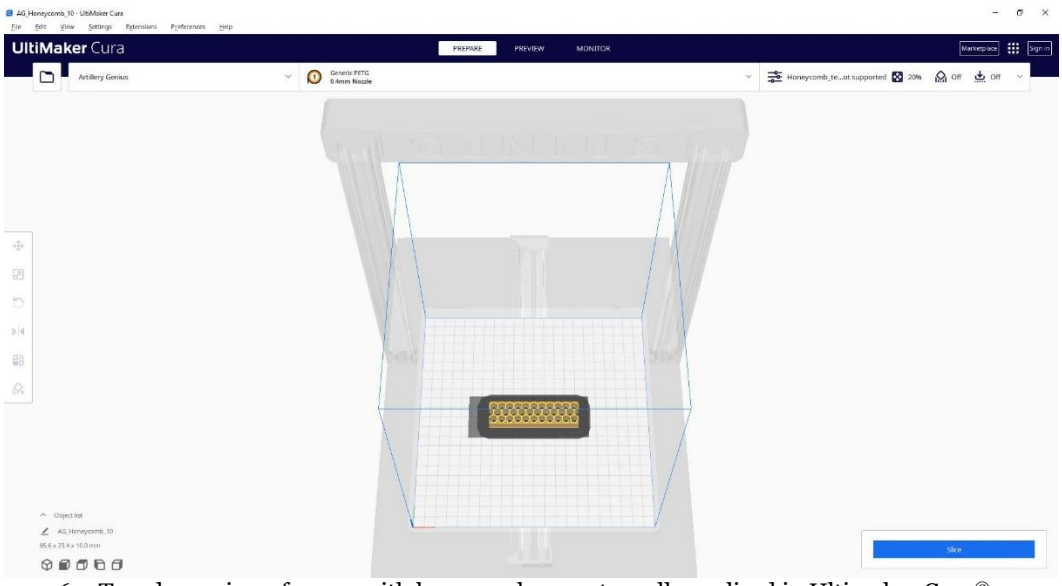

Figure 3.6 – Top-down view of a core with hexagonal geometry cells as sliced in Ultimaker Cura©.

At this point, having selected the printer and core designs, all that is necessary to slice the core designs is to define the ideal printing settings; a configuration file with settings optimised for the used material and machine was developed by Fernandes et al. [29]. This way, the only adjustments necessary to the printing were related to the geometries of the cores and their size. As such, adjustments were made to the printing speed, retraction speed, and retraction distance: by reducing these parameters, the prints were found to be more accurate; at the same time,

excessive speed reduction resulted in longer printing times and, eventually, was found to even decrease the print quality as well. Once these parameters were balanced so that the test prints yielded acceptable results (both in terms of accuracy and speed), the final slicing and printing was carried out (Figure 3.7).

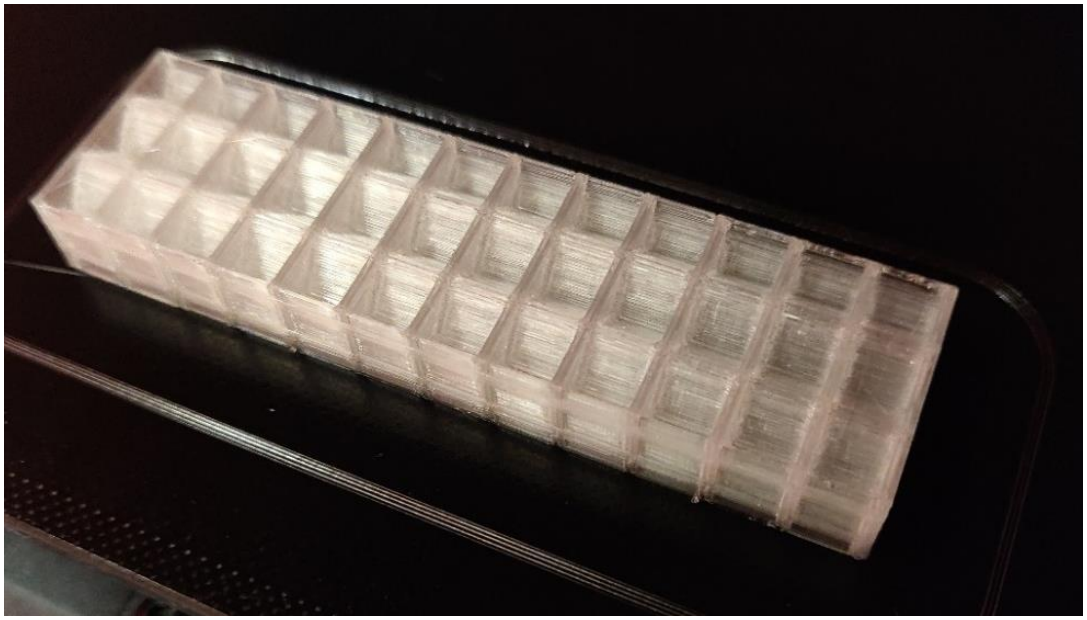

Figure 3.7 – A cubic-celled core printed with the optimised parameters.

To further optimise printing times, multiple cores were sliced and printed together (Figure 3.8).

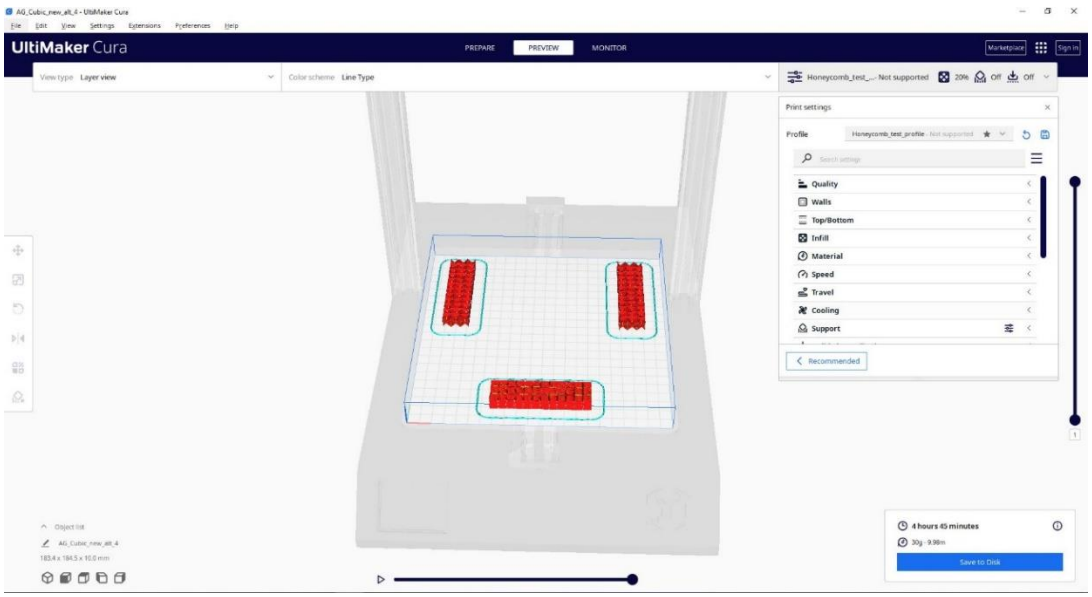

Figure 3.8 – Top-down view of three sliced cores with cubic geometry cells in Ultimaker Cura©.

Note that although these cores were printed sequentially – i.e. not simultaneously – printing this way still allows for significant time saving by reducing the number of times the printed parts and printing bed have to be cooled down for removal and then warmed up again for the next print. Printing three cores at a time means the time spent on these tasks is reduced to a third when

compared to individual printing. Considering that a printed piece would take up to 10 minutes to cool down before any attempt was made to remove it, and that more than 30 cores were being produced, these time savings were rather significant. This process is repeated for every core until there are enough to produce the needed number of samples, with some to spare in case of previously unnoticed defects (Figure 3.9).

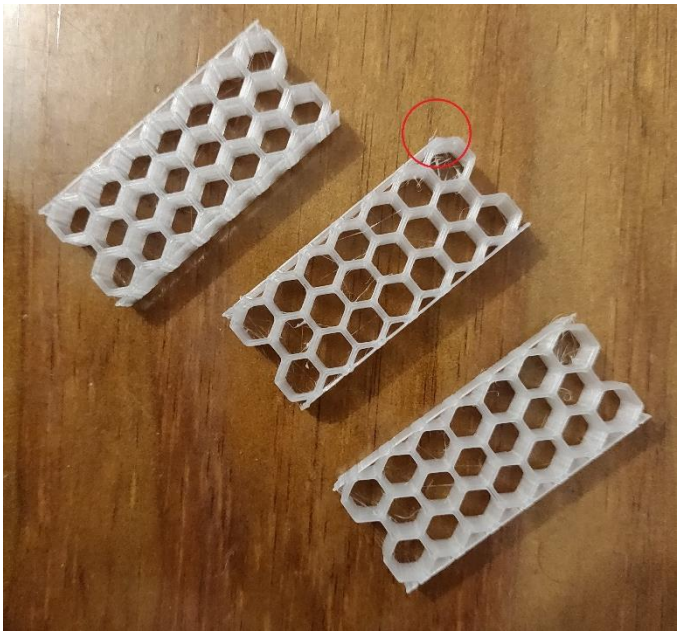

Figure 3.9 – Three hexagonal-celled cores; notice the defective skin at the top of the middle core.

3.1.2. Skins

For the skins, both a sufficient flexibility and conductive capability are needed to achieve both correct loading of the full unit and piezoresistivity. Thus, a decision was made to produce a carbon nanotube-doped fibreglass composite. The choice of fibreglass in lieu of carbon fibre – which would be the chief alternative to fibreglass – helps to minimize abnormalities in the electrical readings of the skins, seeing as fibreglass is non-conductive and as such, unlike carbon fibre, does not muddle the electrical behaviour of the skins, which is largely enabled by the carbon nanotubes inside the matrix. Another advantage of this choice is that they allow, first and foremost, for the direct health monitoring of the resin, which typically sees failures before the fibres. With the materials established, an initial attempt was made to produce the skins.

First off, the fibreglass sheets are cut to size from 195 g/m² fibreglass taffeta (1195 P from Rebelco), first into a 25-mm-wide piece (with the length of the original roll, that is, 80 mm), then into squares with a 25 mm side (Figure 3.10).

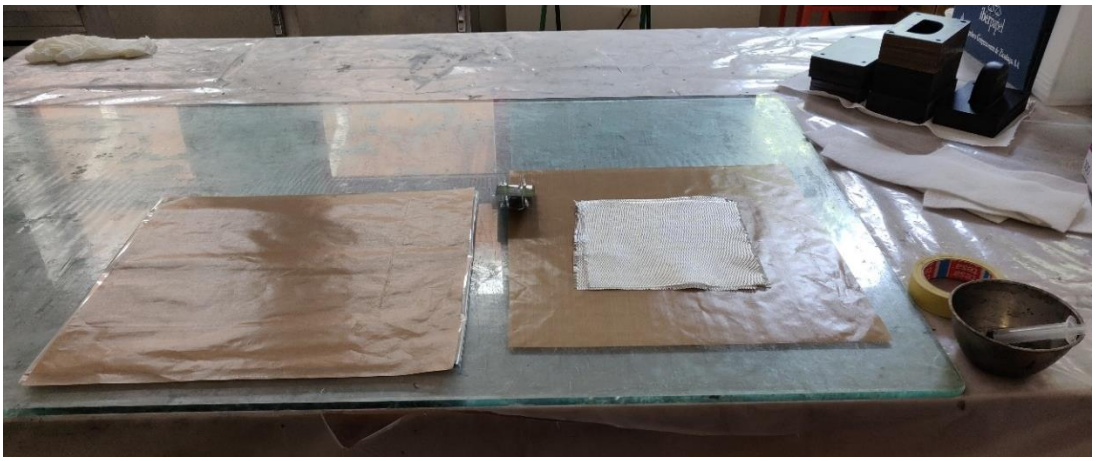

Figure 3.10 – Fibreglass sheets cut into squares and ready for the layering process.

Four of these squares were produced; this number of layers was deemed ideal for achieving an adequate balance of stress and rigidity – enough stress to act the part of a sandwich composite skin, but not so rigid that it prevents bending. (that number would prove to be less than ideal) After this step, the preparation of the resin began: an estimated amount of resin was measured into a cup (in this case, 100 g of resin were determined to be sufficient). Then, the carbon nanotubes (Nanocyl© NC7000 Multiwall carbon nanotubes, Figure 3.11a) were added to the resin (Sicomin© SR8100 epoxy resin Figure 3.11b): the amount was determined to be a 0.5 % of the total mass of both the resin and the hardener, which was not yet added at this stage because the nanotubes would need to be fully incorporated into the resin beforehand. Since the amount of hardener (Sicomin© SD8824 standard hardener, Figure 3.11c) needed was 22 % that of the resin in mass, i.e. 22 g of hardener, a 0.61 g of carbon nanotubes would be necessary.

Figure 3.11 – The three components that make up the resin mixture: a, carbon nanotubes; b, resin; c, hardener; reproduced from[30], [31].

To fully integrate the nanotubes, the resin-nanotube mixture was partially submerged in cold, iced water in an ultrasonic bath (Argolab© AU-65), with an overhead stirrer (Labbox STIV-020-001) running at a 1100 rotations per minute continuously for one hour (Figure 3.12). Afterwards, the mix was removed from the bath, and a probe (Qsonica© Q125 Sonicator) was dipped into the cup and ran for one minute. Finally, the mix was returned to the cold-water tub for another hour (Figure 3.8). Once that hour has elapsed, the hardener was gradually added to the resin mixture, while blending at 300 rotations per minute for 5 minutes.

Figure 3.12 – Resin/Carbon nanotube blend undergoing mixing.

Ideally, once the resin and hardener are joined, the composite should be put in vacuum and under pressure as fast as possible (while the resin/hardener reaction has not been completed, and the mixture remains malleable). A vacuum bag was cut and sealed on all but one side, large enough to fit the 25×25 mm composite, with some added space. A cardboard square was also prepared, to aid in transporting the soft composite into the vacuum bag. As soon as the resin is ready, the layering process begins: first a small dose of resin is dropped over a sheet of PolyTetraFluoroEthylene (PTFE) to prevent sticking, then a single layer of fibreglass is set over it.

Then the resin is manually spread through the fibreglass until it is covered entirely. The resin is scraped over the fibreglass in an outwards motion, in “horizontal” and “vertical” strokes (from the user’s point of view). This step must be done with great care, as otherwise the fibres may be pulled out of place which is, naturally, detrimental to the composite’s structural integrity. Once finished, these steps are repeated for the other fibreglass sheets, except that the sheets are set first, and the resin is dosed over them afterwards. Once all layers are set, the entire bundle is surrounded with double-layered felt barriers (to absorb any excess resin), and put inside the vacuum bag, which was then sealed fully once the vacuum nozzle was put in place (Figure 3.13).

Figure 3.13 – Composite bundle, prior to being inserted into the vacuum bag.

The bag is then placed on the hydraulic press and connected to the vacuum chamber (BACOENG©, attached to a VEVOR© 3CFM vacuum pump), which is run for 10 to 15 min. During this process, a quadrangular metal weight was set over the bundle to flatten the surface of the composite and displace any remaining bubbles from it – preventing pitting on the surface and helping to distribute the resin more evenly. The vacuum machine is then turned off and the composite is compressed for twenty-four hours and then placed in an oven (Carbolite Gero© PF30 fan convection laboratory oven) set at 40 degrees Celsius for another 24 hours to finalise the curing process. The composite skin was then cut into the desired size, and electrodes – in the form of copper wire – were fixed to the outer surface of the composite skins with a layer of conductive paint (MG Chemicals© 842AR Super Shield Silver conductive paint) corresponding to a 5×10 mm area for each electrode, both of which were spaced 15 mm away from the skin's halfway point, and 20 mm from the nearest endpoint (see Figure 3.14).

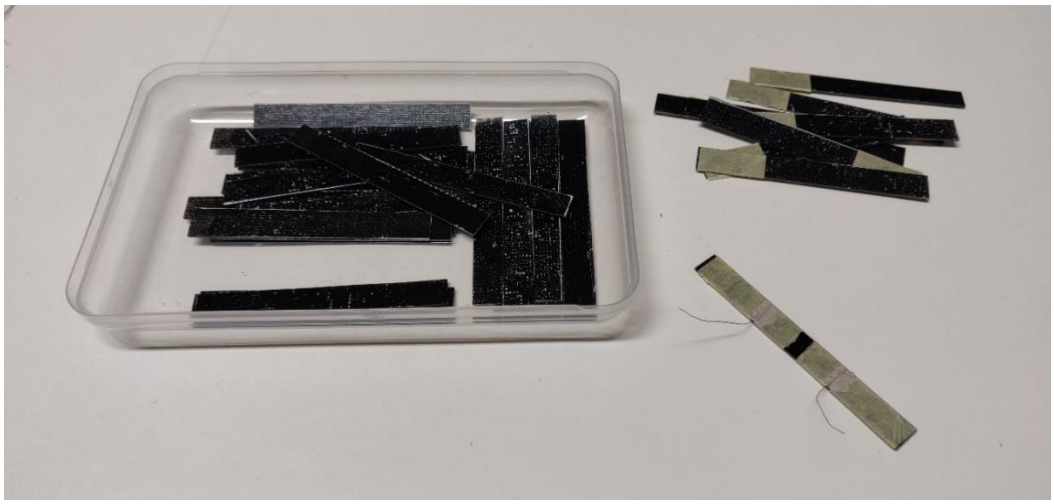

Figure 3.14 – Composite skins at different preparation stages; note the finalised skin in the bottom right of the picture.

Finally, the skins were attached to the printed cores with another dose of resin, resulting in the finalised testing samples (Figure 3.15).

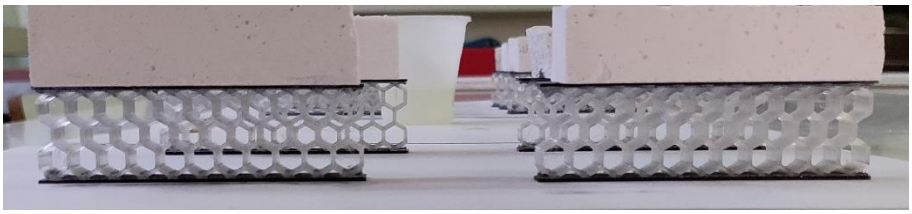

Figure 3.15 – Testing samples undergoing final assembly; weights were placed over them to promote better core/skin adhesion.

3.2 Experimental Procedure

Following their construction, the testing samples were subjected to three-point bending tests; a Shimadzu Corporation© Autograph AGS-X universal testing machine (Figure 3.16a) was used, mated to a desktop computer running Trapezium X v1.5 (also from Shimadzu) (Figure 3.16b) for the acquisition of the mechanical readings and a Keysight Technologies© 34461A digital multimeter (Figure 3.16c) for the electrical readings.

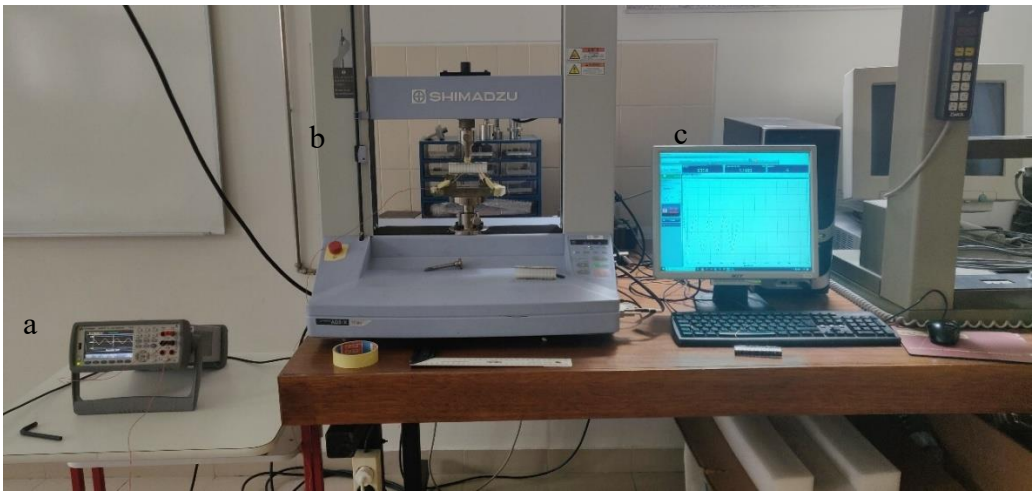

Figure 3.16 – The three main components of the testing apparatus: a, multimeter; b, testing machine; and c, desktop computer.

There were three types of tests: a static bending test, where the samples were continuously deformed into their plastic behaviour, were they sustained damage; a cyclic bending test, where the samples were limited to their elastic behaviour, to assess the replicability of their properties over the length of 10 cycles; and another cyclic bending test, with the addition of dwell periods, to observe the relaxation of stresses and other stress-related phenomena.

To ensure testing validity and proper data acquisition the tests were conducted in accordance with an international standard (as stated previously). While a dedicated sandwich constructions standard would normally be preferred – the ASTM (American society for Testing Materials) C 393 for instance – the cell direction for the core necessitates a significantly tall sample, which invalidated the samples in relation to dedicated sandwich standards. Because reducing the cell dimensions even further is prevented by printing limitations, and printing larger samples is unviable due to time, material and machine-related scale constraints, a different standard was selected: the ASTM D 790 “Standard Test Methods for Flexural Properties of Unreinforced and Reinforced Plastics and Electrical Insulating Materials”. As stated, the samples undergo loading in a three-point bending configuration (Figure 3.17).

Figure 3.17 – A hexagonal-celled sample ready for the three-point bending testing.

Where:

b = beam width, mm,

d = beam thickness, mm,

l = beam length, mm,

L = support span, mm and

P = load, N.

The equipment used for these tests then acquires data for the load (force) and mid-span deflection (displacement), arranged in an Excel-compatible format. From these values, the stress (stress, σ, see Equation 3.1) and strain (ε, see Equation 3.2) at the mid-point can be obtained.

$$\sigma = \frac{3 \times F \times L}{2 \times b \times d^2} \qquad 3.1$$

Where:

σ = stress, MPa,

F = force, N and

L, b and d carry over from Figure 3.16.

$$\varepsilon = \frac{6 \times L \times d}{L^2} \times 100 \qquad 3.2$$

Where:

ε = strain, % and

L and d carry over from Figure 3.16.

Both stress and strain are then used to plot a curve in order to facilitate analysis of the test results, such as the example provided below (Figure 3.18).

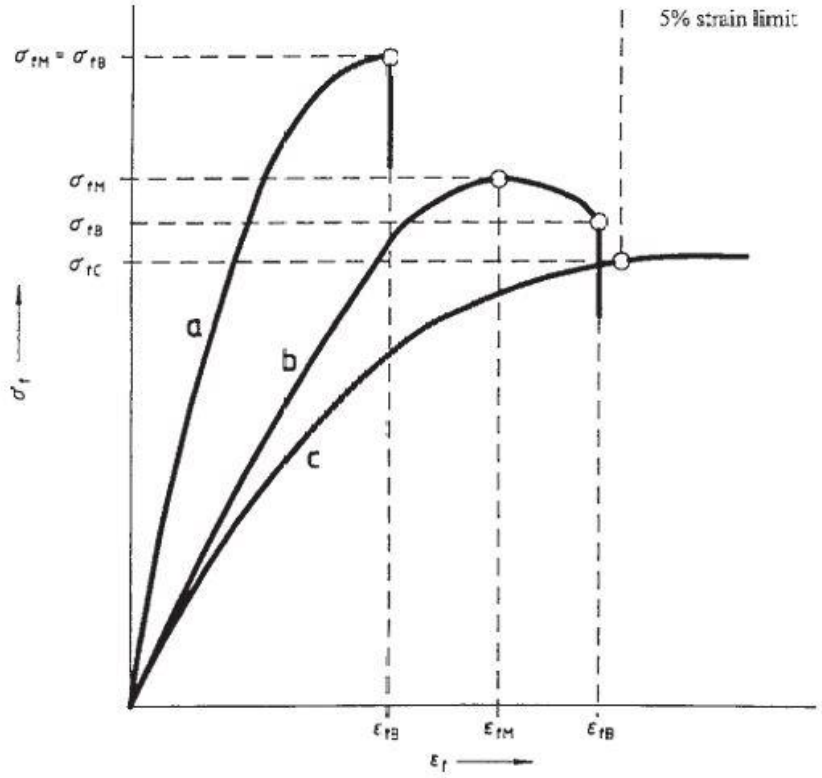

Figure 3.18 – Stress/strain examples: typical stress/strain curves, reproduced from [32].

Note that in this particular case, the specimens are expected to break post-yield and no sooner than the 5 % strain limit, therefore the c curve (see Figure 3.18 above) is estimated to be the most representative of the three for these tests. The plotted curve is expected to fully display elastic deformation and yield point as well as the plastic deformation at least partially, if not in full. Additionally, the elastic deformation is expected to display a Hookean Region, i.e. a region where Hooke's Law applies, where stress and strain are proportional and therefore the curve is linear. This Hookean Region ends before the yield point – around which linearity is not observed, before or after – and is preceded by a toe region which as stated in standard D 790 «does not represent a property of the material» and «is an artifact caused by a take-up of slack and alignment or seating of the specimen» [32]. In the Hookean region the modulus of elasticity (or elastic modulus / Young's modulus) can be accurately determined from the division of the stress by the strain (Equation 3.3). Note that stiffness is predicated by the elastic modulus; increased stiffness corresponds to high values of the elastic modulus, and vice-versa. Also note that the scope of the tests that the composite samples underwent is largely related to their elastic deformation: the elastic modulus is crucial to their characterisation (and will be featured extensively).

$$E = \frac{\sigma}{\varepsilon} \qquad 3.3$$

Where E is the elastic modulus (MPa), and the stress, σ (MPa) and strain, ε (%) carry over from Equation 3.1 and Equation 3.2 respectively.

Certain parameters must be set in order to carry out the tests; since the machine will displace the specimen's midpoint, those would be the displacement limit and the testing speed (i.e. the rate of displacement per unit of time). As is stated in the ASTM D 790 standard, the speed is to be set to "2 mm/min or less". As such, the 2 mm/min speed was chosen for these tests, to avoid a lengthy testing process. The limit for the displacement (and by extension strain) is largely arbitrary during the static tests, since the main points of interest are the elastic deformation and the region around the point of yield (and the point itself), however there is also an interest in comparing the behaviour of the different core cell geometries during the plastic deformation, namely to estimate the composites' capability to absorb energy during both elastic and plastic behaviour. As such those tests were determined to end no sooner than the 30 % strain mark. For the cyclic tests, the strain was limited to a maximum of 80 % of the strain at the point of yield for each geometry; this was done to prevent the samples from entering plastic deformation during those tests. This limit was also used for the tests with dwell; these tests include the addition of a dwell to the moments the samples reached the point of zero strain, as well as the specified maximum strain.

Another matter is the electrical aspect of these tests. The multimeter provides readings of the electrical resistance in Ohm, Ω. However, the variations in the electrical resistance are more relevant than their absolute value, so facilitate the reading of the data, the relative electrical resistance is determined (Equation 3.4) [33], [34].

$$\frac{\Delta \mathrm{R}}{R_0} = \frac{R_f - R_0}{R_0} \times 100 \tag{3.4}$$

Where:

$\frac{\Delta R}{R_0}$ = relative electrical resistance, %,

R_o = initial electrical resistance, Ω, and

R_f = final electrical resistance, Ω.

Now, to determine the piezoresistive sensitivity – given by the electrical resistance readings – to the mechanical deflection of the samples, the gauge factor can be determined (Equation 3.5).

$$GF = \frac{\frac{\Delta \mathrm{R}}{R_0}}{\varepsilon} \tag{3.5}$$

Where:

GF = gauge factor and

$\frac{\Delta R}{R_0}$ and ε carry over from Equation 3.4 and Equation 3.2 respectively.

With that, all relevant values can be extracted from the experimental data and processed for further analysis together, after the tests are concluded.

4. Results, Discussion

4.1 Results

As the primary objective of these tests was the mechanical and electrical characterisation of each structural topology, the results were split into 3 sections – hexagonal, auxetic and cubic, each for the corresponding topology. Within each section, the characterisation begins with the three-point bending static testing, followed by cyclic testing, and then a representative cyclic testing with dwell, as stipulated in section 3.2.

4.1.1. Hexagonal

Starting with the hexagonal topology, a stress versus strain graph of a representative sample, along with photographs from the tests, is presented underneath (Figure 4.1).

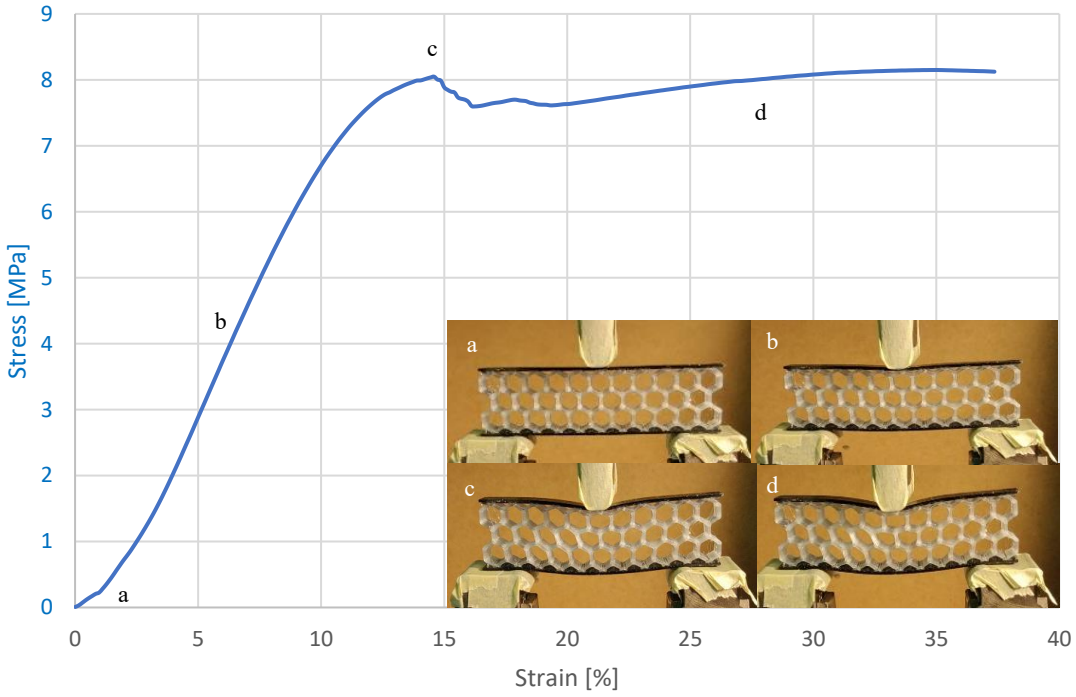

Figure 4.1 – Representative three-point bending stress versus strain graph for hexagonal topology with corresponding photographs of different test moments.

By observing these graphs, an initial adjustment phase can be seen (a) – as parts of the setup and samples both settle into each other – at around a 0.7 % strain and 0.17 MPa stress. At this point the samples remain visually unchanged.

This is followed by elastic behaviour, as displayed by a (mostly) linear section of the graphs in accordance with Hooke's Law (b), and the gradual deformation of the samples, especially for the cells in the middle row. This lasts until around the 9 % strain (or 6.1 MPa stress) mark and then gives way as the increase in stress trails off to the point of maximum stress (c) at about 14.6 % strain and 8.0 MPa stress.

After this, stress begins to decrease, then plateaus and, eventually, will begin to increase again as densification develops (d). During these stages, the cells continue to deform irregularly and the difference in deformation becomes more accentuated, with the middle row deforming the most and the bottom row the least. The top skin also becomes heavily deformed due to the compressive stress, particularly when compared to the bottom one which is subject to tensile stress.
The previous graph is then followed up by a new one, representing the same curve within the 0-30 % strain interval, along with the respective absorbed energy (Figure 4.2).

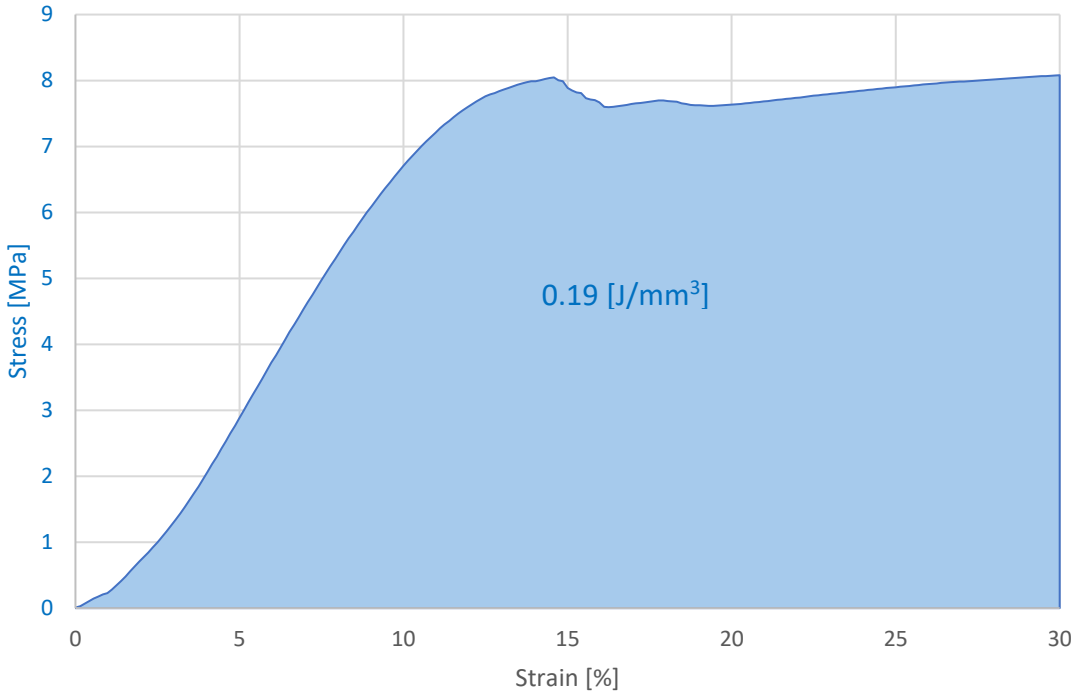

Figure 4.2 – Representative three-point bending stress versus strain graph up to 30 % strain and corresponding storage of energy for hexagonal topology.

This is made possible by calculating the area under the graph (as detailed in section 3.2) up to a 30 % strain, to make an estimation of the energy absorbed by the samples throughout both the elastic behaviour and the beginning of the plastic phase – the choice of a 30 % strain threshold was made to provide a better comparison across topologies, by allowing the measurement of the same range of behaviours for all three topologies.
For the hexagonal samples, the result was a 0.19 J/mm^3 estimated absorbed energy until 30 % of strain.
Furthermore, electrical resistance readings were also taken from the top skin during the previous tests. So, stress versus displacement and relative electrical resistance – as calculated in section 3.2 – versus displacement charts were plotted for a representative sample (Figure 4.3).

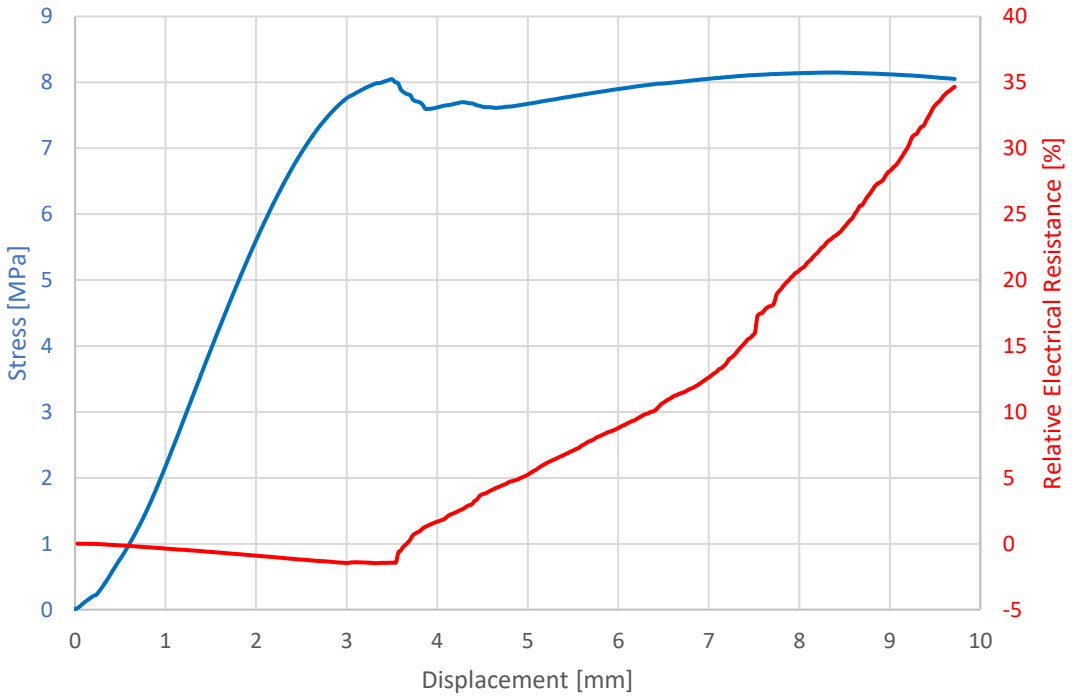

Figure 4.3 – Representative three-point bending stress versus displacement up to 10 mm and corresponding relative electrical resistance for hexagonal topology.

As expected, sudden changes in electrical resistance, and stress, correspond to each other, with a sharp increase in electrical resistance for each sharp decrease in the stress.

After the abrupt increase near the 3.5 mm displacement mark, the relative electric resistance increases more drastically, likely due to accumulating damages on the upper skin which, as seen in Figure 4.1 (d), already suffered significantly by this point. This increase in the relative electrical resistance continues until the end of the test.

Looking now at just the 3-4 mm bracket of displacement, the correlation between stress and relative electrical resistance around the inflection point is easier to observe (Figure 4.4).

As evidenced above, most of the graph for the relative electrical resistance displays linearity before the inflection point. Afterwards, the graph climbs considerably as the elastic behaviour comes to an end. Assuming any delays in the electric response are accounted for, this represents an alternative means of determining the end of the elastic behaviour for the samples.

The evaluation of the elastic behaviour in cyclic testing and corresponding electrical response, via relative electrical resistance can be carried out now, resulting in the following graph for the cyclic testing of the hexagonal topology (Figure 4.5).

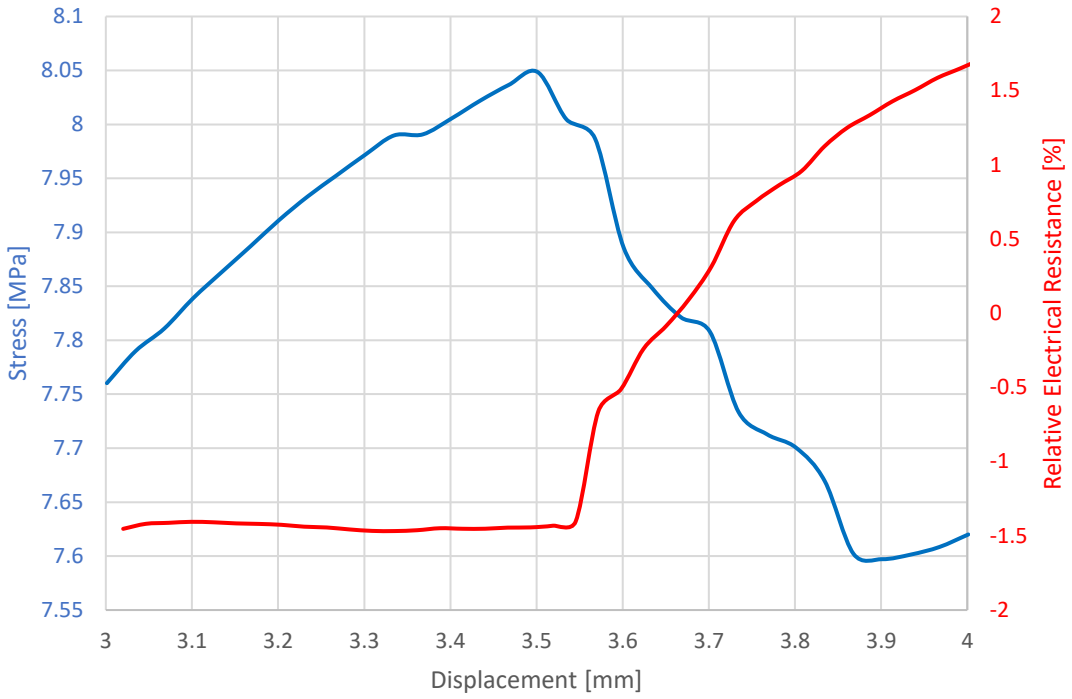

Figure 4.4 – Detail for the first 2 mm of the three-point bending stress versus displacement graph and corresponding relative electrical resistance for hexagonal topology.

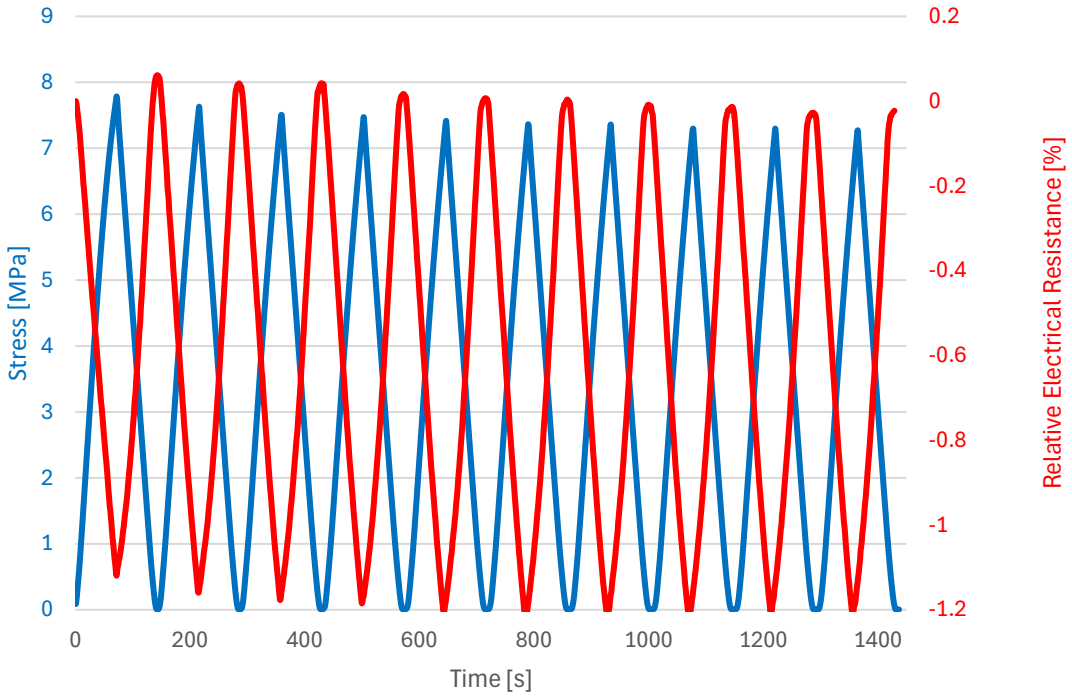

Figure 4.5 – Representative cyclic stress and relative electrical resistance in function of the time for hexagonal topology.

For the hexagonal topology (Figure 4.5), the relative electrical resistance displayed stable behaviour, with the more pronounced noise occurring at the end/start of a cycle – likely the result

of the sample being released and accidentally moved during the tests. Note also that the relative electrical resistance develops inversely to the stress – i.e. as the stress increases, the relative electrical resistance decreases and vice-versa. Therefore, this sample can be said to display a negative piezoresistivity. In the cyclic tests the strain increases and then decreases at a constant rate for each cycle. The electrical resistance, which is also displayed along the stress response, varies inversely to the latter, which behaves similarly to the strain. There also seems to be a tendency for both the maximum and minimum relative electrical resistance to decrease with each cycle, as is the case with the maximum stress; for instance, when comparing the first and second cycles the maximum stress decreases 2.0 % and the maximum and minimum relative electrical resistance decrease 32 % and 3.6 % respectively. Additionally, the difference between maximum and minimum relative electrical resistance is 1.2 % for the first, fifth and tenth cycles; as such, it may be concluded that the range of relative electrical resistance within each cycle remains constant. Otherwise, the graph displays a stable behaviour.

To better examine the accuracy of the electrical response, particularly at the limits of each cycle, the previous figure is also represented within a slimmer time frame, throughout the first and second cycles (Figure 4.6).

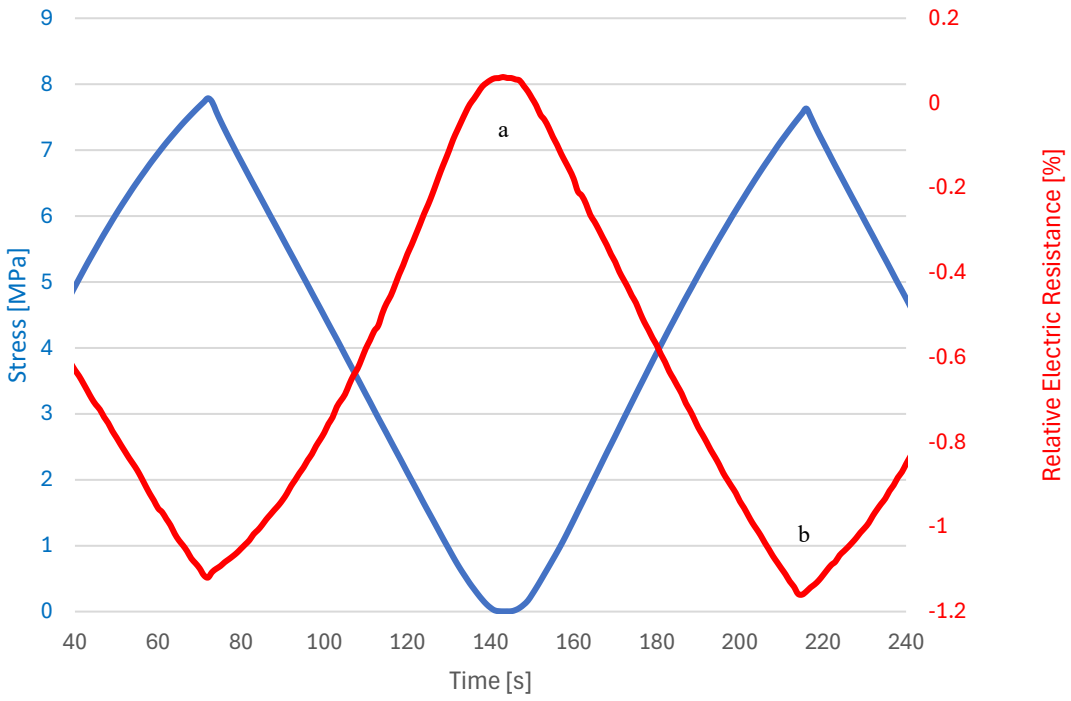

Figure 4.6 – Detail for the first and second cycles from the representative cyclic stress and relative electrical resistance in function of the time for hexagonal topology.

Upon further inspection, the graph is non-linear between cycles, (a); this is due to the structure undergoing residual deformation. Note that the corresponding turning points are more pronounced mid-cycle (b) than between cycles.

Finally, a new graph was created to observe how the stress deteriorated along the tests, by aligning maximum stress with each cycle; the gauge factor – as determined according to the procedure described in 3.2 – is also displayed, showcasing the quality of the electrical response (Figure 4.7).

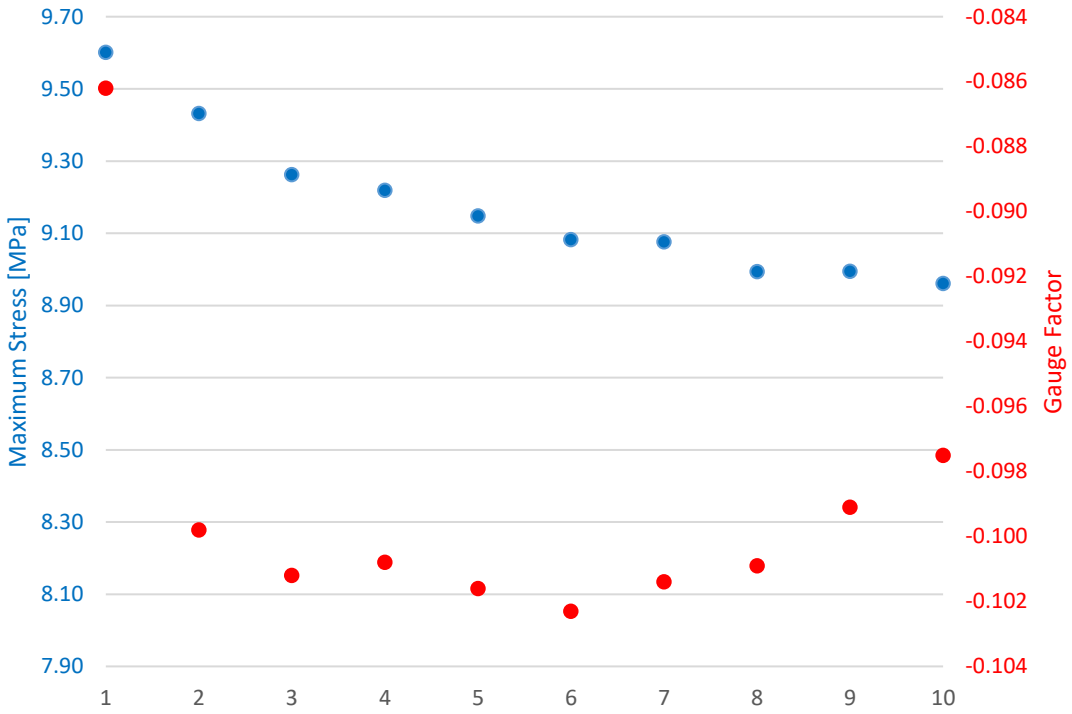

Figure 4.7 – Evolution of mean maximum stress per cycle with corresponding trend-line and gauge factor for hexagonal topology.

Upon listing the maximum stress readings, a nearly constant reduction in value can be observed, starting at 9.6 MPa for the first cycle, and ending at a 93.3 % of the original value by the tenth cycle, thereby confirming the initial assertion that the maximum stress would decrease with ongoing cycles.

As for the gauge factor, the value for the first cycle can be discarded as initial deformations lead to a poorer quality for the electrical resistance readings. Otherwise, after the initial deformation, the values span less than a 0.005 gap and display great repetitiveness, indicating a good signal quality.

The former tests are then followed by a cyclic test with the addition of a dwell period (a period of constant loading at the maximum and the minimum strains, lasting 30 seconds each), resulting in the graph bellow (Figure 4.8).

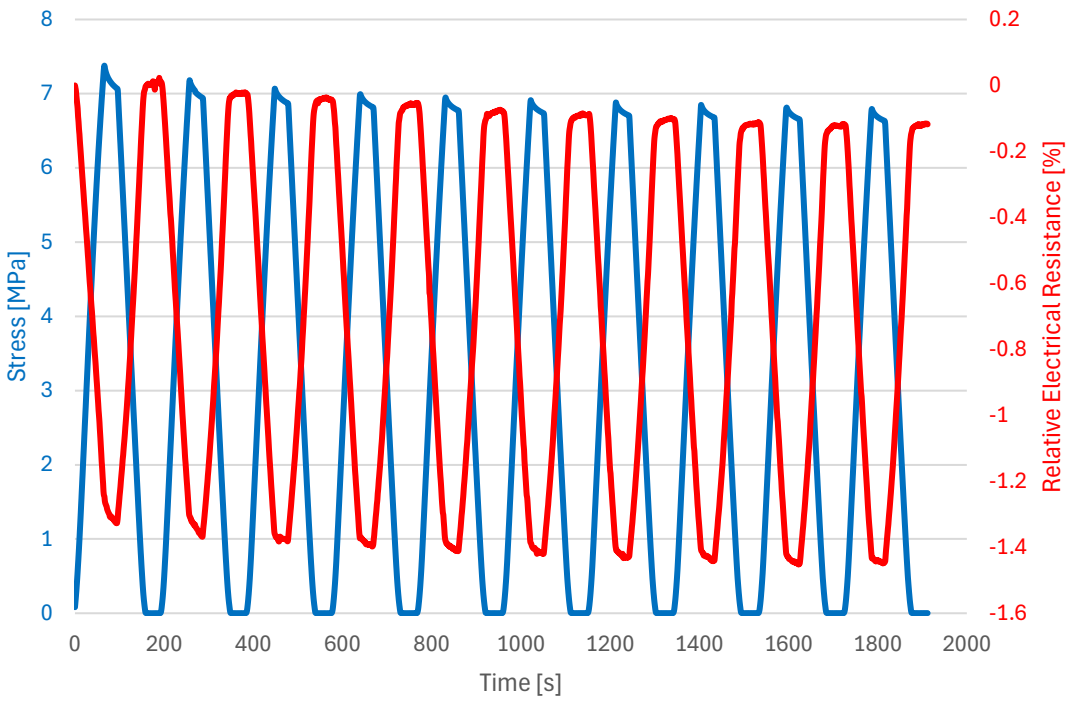

Figure 4.8 – Representative cyclic stress and relative electrical resistance in function of the time for hexagonal topology with dwell.

With the inclusion of a dwell time, the new cyclic tests yielded much of the same behaviour present during the previous ones, with the added benefit of allowing the observation of the structural residual deformation mid-cycle, and corresponding relative electrical resistance. And in fact, the graph clearly shows a dip in both the relative electrical resistance and stress, while strain remains constant. There is a perceived tendency for the stress and relative electrical resistance to decrease during the intra-cycle dwell periods, and the evolution of the relative electrical resistance appears to be proportional to that of the stress, suggesting that there is good correlation between both.

While some divergent behaviour is evident in Figure 4.8, differences from the previous cyclic tests can be observed in better detail, in the same graph, when within a smaller time frame – for instance, during second cycle (Figure 4.9).

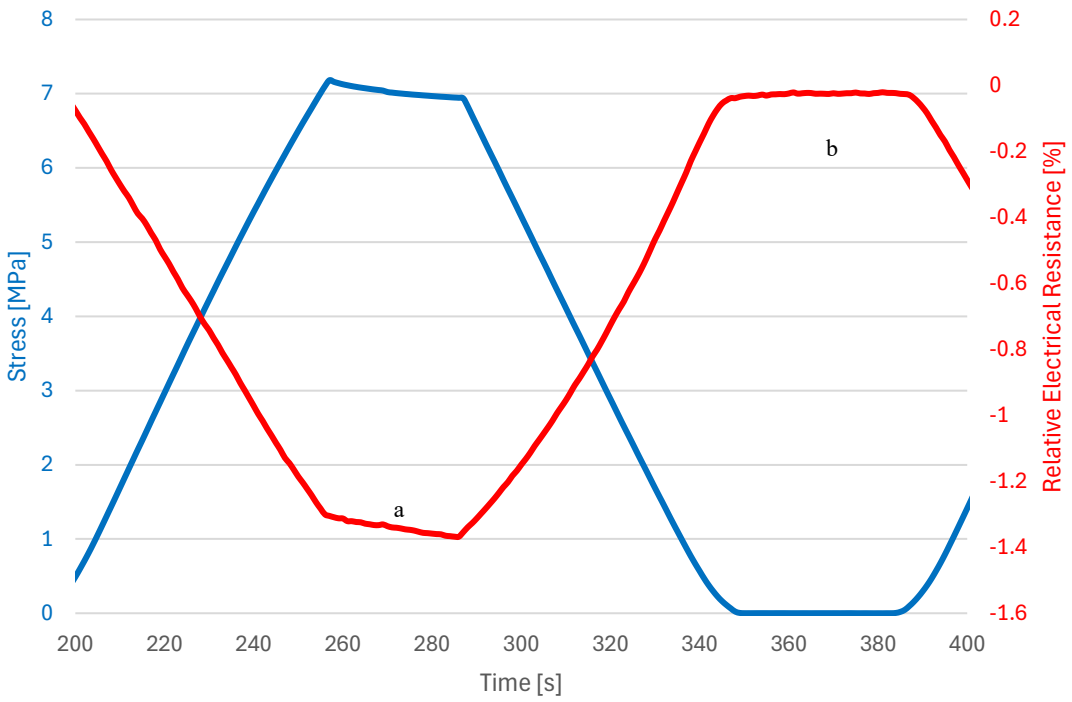

Figure 4.9 – Detail for second cycle from the representative cyclic stress and relative electrical resistance in function of the time for hexagonal topology with dwell.

Indeed, as strain maintains a constant value, the relative electrical resistance is observed to decrease even further relatively to the initial value (a). The same sort of change is also present for the stress, during the same period. At times, the relative electrical resistance increases a 4.5 % over the initial value, by the end of a dwell. Likewise, stress suffers reductions of up to 3 % throughout these periods. And as before, there is also more noise between cycles (b) than for the rest of the test.

Finally, a summary of some values is compiled within a table for the static and cyclic tests (Table 4.1), and for the cyclic tests with dwell (Table 4.2), for ease of reference and reading (this will be useful during the next subsection, to discuss results across topologies).

Table 4.1 – Summary of data collected from the three-point bending static and cyclic testing for hexagonal topology.

Tests	Values	Mean	Std.Dev.
Static testing	Max. Stress [MPa]	7.0	0.6
	Elastic Modulus [MPa]	72.6	3.9
	Absorbed Energy [J/mm3]	0.16	0.01
1st cycle	Max. Stress [MPa]	8.1	0.3
	Elastic Modulus [MPa]	82.4	3.5
5th cycle	Max. Stress [MPa]	7.7	0.3
	Elastic Modulus [MPa]	78.6	3.3
10th cycle	Max. Stress [MPa]	7.6	0.3
	Elastic Modulus [MPa]	77.0	3.2

Table 4.2 – Summary of data collected from the representative cyclic testing with dwell for hexagonal topology.

Dwells	Values	
1st dwell	Initial Stress [MPa]	7.3
	Final Stress [MPa]	7.1
	Initial Elastic Modulus [MPa]	80.7
	Final Elastic Modulus [MPa]	77.7
5th dwell	Initial Stress [MPa]	6.9
	Final Stress [MPa]	6.8
	Initial Elastic Modulus [MPa]	76.2
	Final Elastic Modulus [MPa]	74.4
10th dwell	Initial Stress [MPa]	6.8
	Final Stress [MPa]	6.6
	Initial Elastic Modulus [MPa]	74.5
	Final Elastic Modulus [MPa]	72.9

4.1.2. Auxetic

Moving onto the auxetic structure topology, the three samples are represented again by a single stress versus strain graph, and corresponding photos (Figure 4.10).

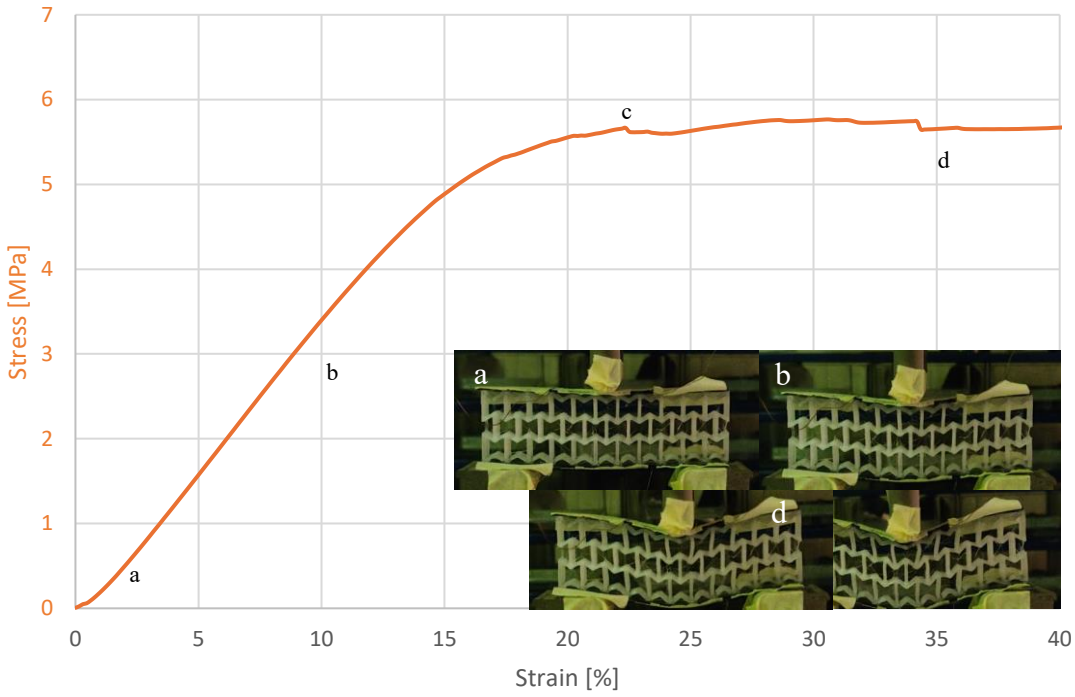

Figure 4.10 – Representative three-point bending stress versus strain graph for auxetic topology with corresponding photographs of different test moments.

Similarly to the hexagonal topology, there is a period of adjustment initially (a), which gives way to the elastic behaviour at around 0.6 % strain (0.09 MPa stress). Visually, there are no observable changes to the samples at this point.

From then until roughly the 13 % strain (4.4 MPa stress) mark, there is a linearity characteristic of the elastic behaviour in accordance with Hooke's Law (b). Around halfway through the elastic phase, the samples have just about begun to bend visually.

At 22.2 % strain the graph reaches a point of maximum stress – 5.7 MPa (c). By this point, the deformation to both skins is observable with ease, and some cells have become deformed, particularly on the top layer and down the middle. While the central cells expand under compression, the cells furthest to the left and right bend.

After that, a very mild decrease in stress is followed by a plateau (d). By now, the samples have deformed even more; in the core, the top centre cell has become particularly more deformed than before.

The previous graph is followed by a new version, with the sample photos removed, to facilitate visualisation of the area under the curve (Figure 4.11).

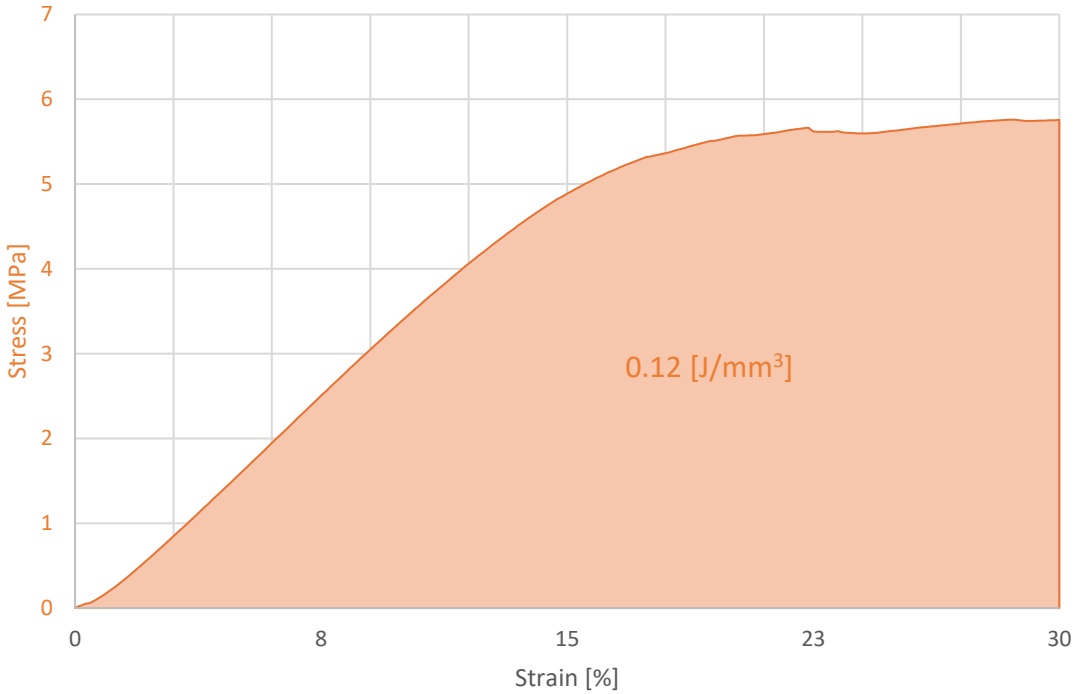

Figure 4.11 – Representative three-point bending stress versus strain graph up to 30 % strain and corresponding storage of energy for hexagonal topology.

As in the hexagonal topology, the area under the curve stands as an estimation for the energy absorbed during the testing, for the elastic behaviour and part of the plastic behaviour – a 0.12 J/mm^3 energy absorbed in this case until 30 % of strain.

As before, stress and relative electrical resistance versus displacement graphs were plotted to assess the electrical response during the static test (Figure 4.12).

Initially, the curves behave linearly and inversely to each other. Both the stress and relative electrical resistance curves display an inflection point at nearly the same displacement, after which the stress curve plateaus and the relative electrical resistance increases. The behaviour displayed both before and after the inflection point is as expected, based on the results from the hexagonal tests.

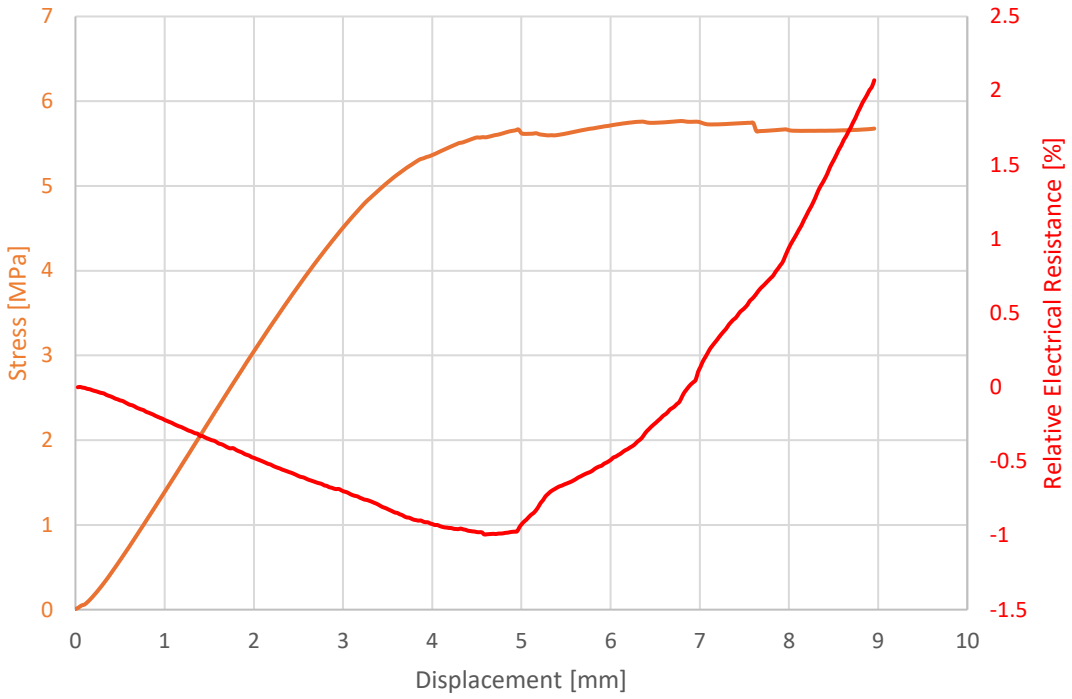

Figure 4.12 – Representative three-point bending stress versus displacement up to 10 mm and corresponding relative electrical resistance for auxetic topology.

To better assess the electrical behaviour around the inflection point, the same graphs are displayed within a smaller displacement frame (Figure 4.13).

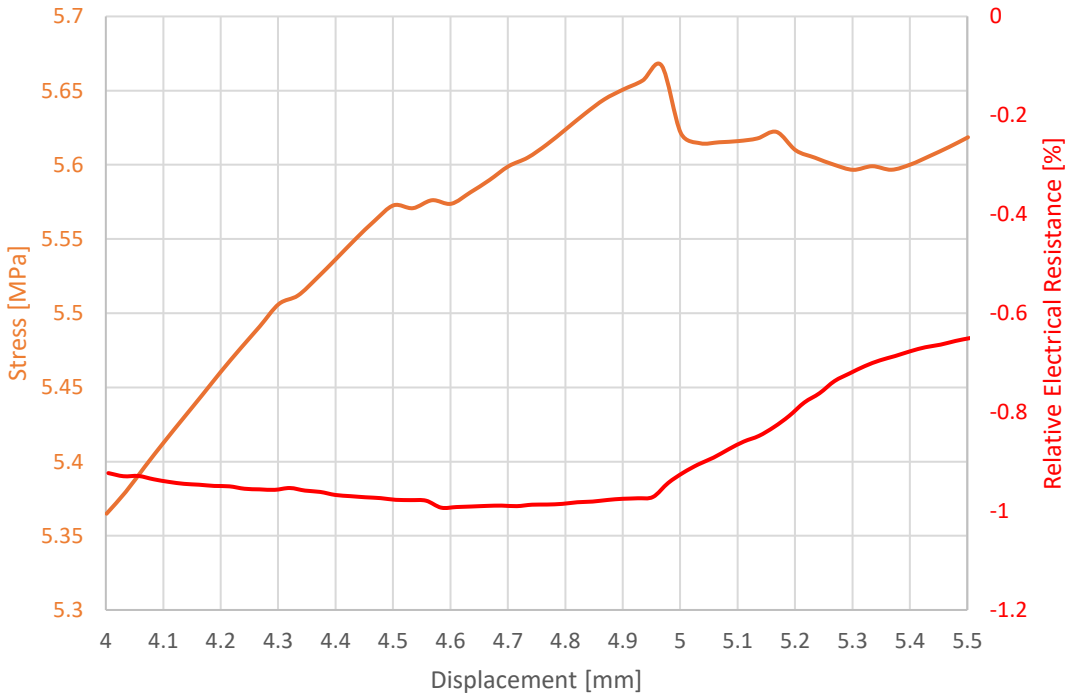

Figure 4.13 – Detail for the 4.5 to 5.5 mm interval of the three-point bending stress versus displacement graph and corresponding relative electrical resistance for auxetic topology.

In this graph, it is possible to see how the relative electrical resistance goes from decreasing to increasing in value just before the 4.6 mm of displacement, just as the stress begins to increase more drastically. The inflection point for the stress curve happens later, between the 4.9 and 5 mm of displacement, at a point of maximum stress. There is also a much greater increase in the relative electrical resistance in this bracket, corresponding to the sharp decrease in stress immediately after the maximum stress.

With the three-point bending static tests completed, the cyclic tests begin, with the elastic behaviour represented by stress and relative electrical resistance in function of the time (Figure 4.14).

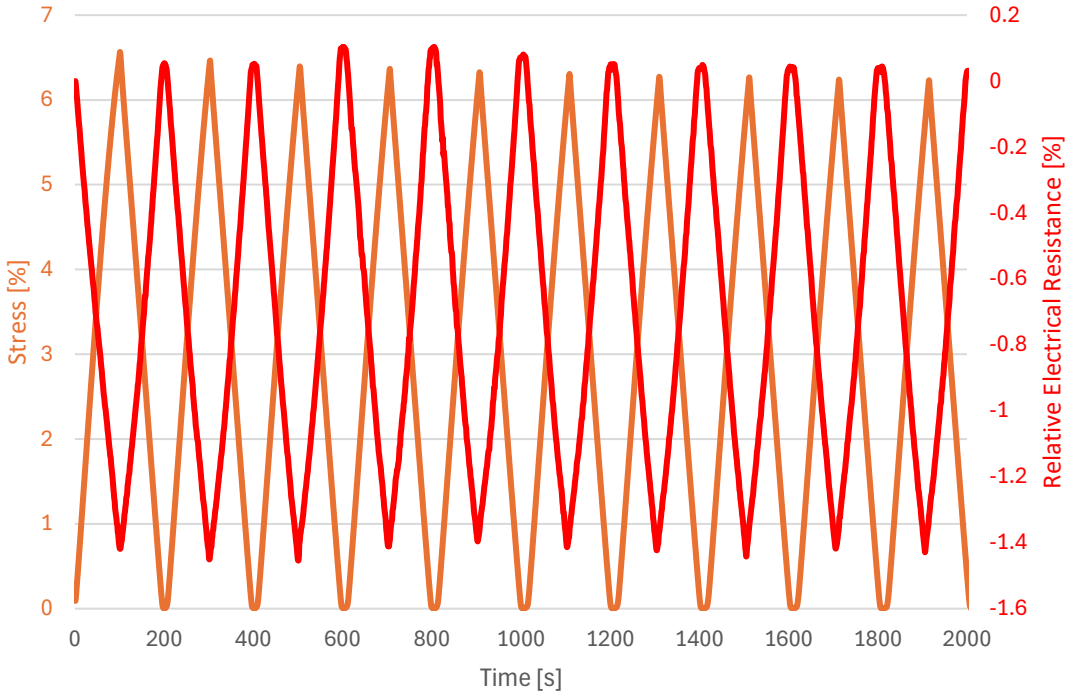

Figure 4.14 – Representative cyclic stress and relative electrical resistance in function of the time for auxetic topology.

Much like the previous topology, the tests proceed with relative stability, with the strain increasing, then decreasing, for each cycle. As before, the stress values change accordingly to the strain, while the relative electrical resistance displays negative piezoresistivity. Noise seems rather negligible in this scope. Although a tendency for the maximum stress and relative electrical resistance to progressively decrease across cycles would be expected, the relative electrical resistance increases from the third to the fourth and fifth cycles instead. Still, it behaves as expected during the other cycles, and the same can be said for the stress. For instance, from the first to the second cycles the maximum stress decreases 1.5 %, while the maximum and minimum relative electrical resistance decrease 2.3 %. The cyclic range for the relative electrical resistance remains a 1.5 % for the first, fifth and tenth cycles. As such, the range can be said to be constant, which is indicative of a consistent electrical response. The rest of the graph can be said to behave nominally.

In order to better examine the stress and electrical response, the previous figure is now shown in a smaller time frame, encompassing part of the first and second cycles (Figure 4.15).

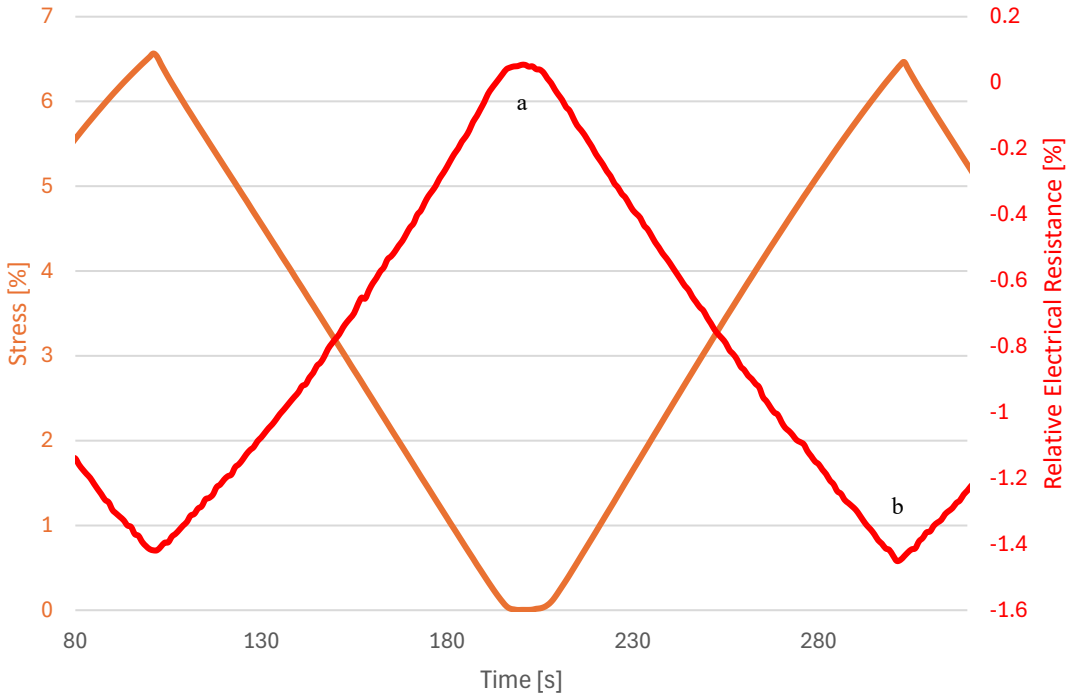

Figure 4.15 – Detail for the first and second cycles from the representative cyclic stress and relative electrical resistance in function of the time for auxetic topology.

With this figure, a contrast can clearly be seen between the inter-cycle (a) and intra-cycle (b) turning points, with the curvature in between cycles being more rounded, while the turning point mid-cycle is sharper and more distinct. As described during the cyclic tests for the hexagonal topology, the reduced linearity inter-cycle may be caused by structural residual deformation, which wouldn't be present during a cycle, hence the sharper point. Note that the quality of the inflection points in the stress curve is congruent with that of the relative electrical resistance curve (i.e. to a rounded inflection in the stress curve corresponds a rounded inflection in the relative electrical resistance and vice-versa).

A new graph allows for a better visualisation of the evolution of the maximum stress per cycle, while also displaying the gauge factor for these tests (Figure 4.16).

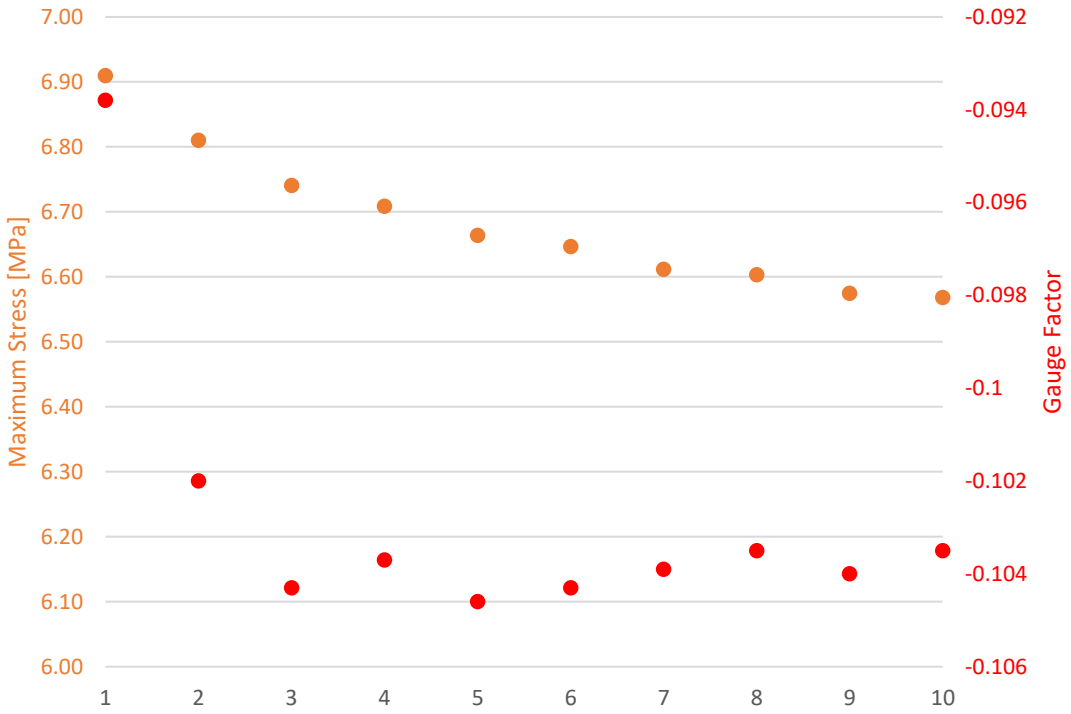

Figure 4.16 – Evolution of mean maximum stress per cycle with corresponding trend-line and gauge factor for auxetic topology.

The maximum stress decreases in value consistently with each cycle and, while starting at a 6.91 MPa in the first cycle, by the final cycle the stress is a 95.1 % of the original value.
All values for the gauge factor, except for that of the first cycle, fit within a 0.003 close gap. Therefore, the stability of the value for the gauge factor throughout the tests and across cycles indicates a good signal quality.

The cyclic tests are again repeated with the additional thirty-second dwell period, yielding the following graph of stress and relative electrical resistance in function of time for ten cycles (Figure 4.17).

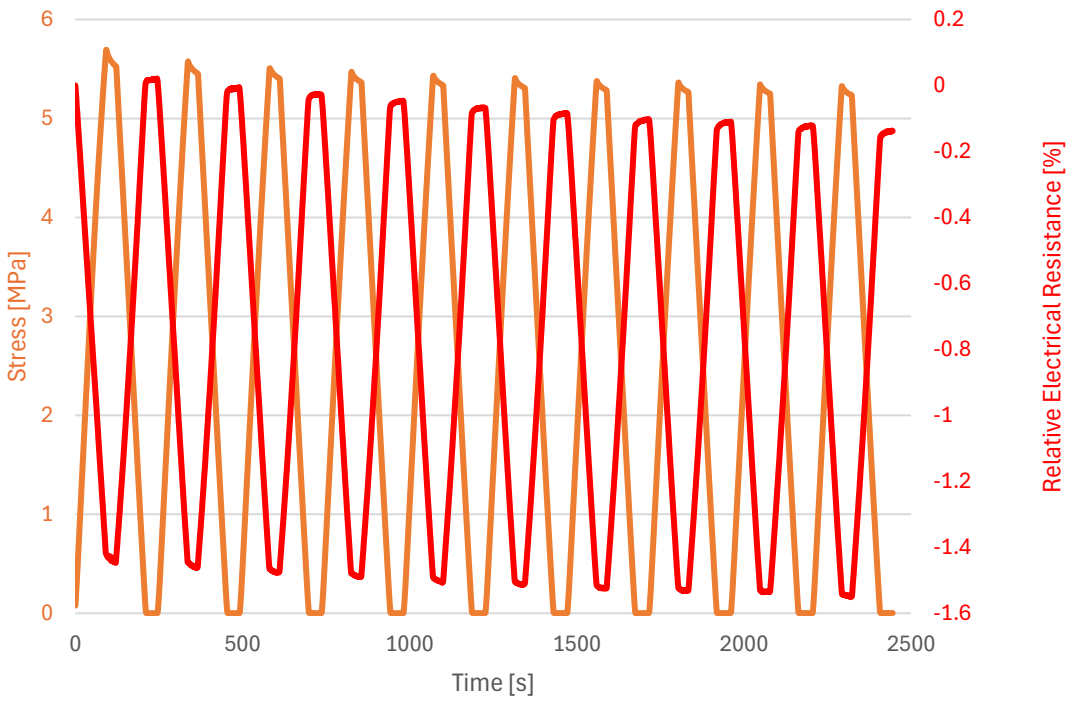

Figure 4.17 – Representative cyclic strain and relative electrical resistance in function of the time for auxetic topology with dwell.

In this case, the effect of the dwell on the relative electrical resistance is much the same as that observed on the hexagonal topology. Both stress and relative electrical resistance decrease during the intra-cycle dwells, and there appears to be a tendency for both values to decrease from cycle to cycle overall. The evolution of the relative electrical resistance seems to follow that of the stress (e.g. in the first dwell both values decrease sharply, while in the last one both values see a milder decrease), which is indicative of a good correlation of mechanical and electrical responses.

A smaller frame of reference allows for a better understanding of the graph profile and the corresponding noise, and so the previous figure is adjusted accordingly (Figure 4.18).

While the dwells are underway, both relative electrical resistance and stress decrease in value mid-cycle (a); in this cycle, the stress decreases a 2.3 %, while the relative electrical resistance sees a 1.1 % decrease. Noise seems rather minimal (particularly compared to other structural geometries) but is nevertheless more pronounced during the inter-cycle dwells (b). Also note the less pronounced evolution of the curve around the beginning and end of the dwell, compared to the former one (a).

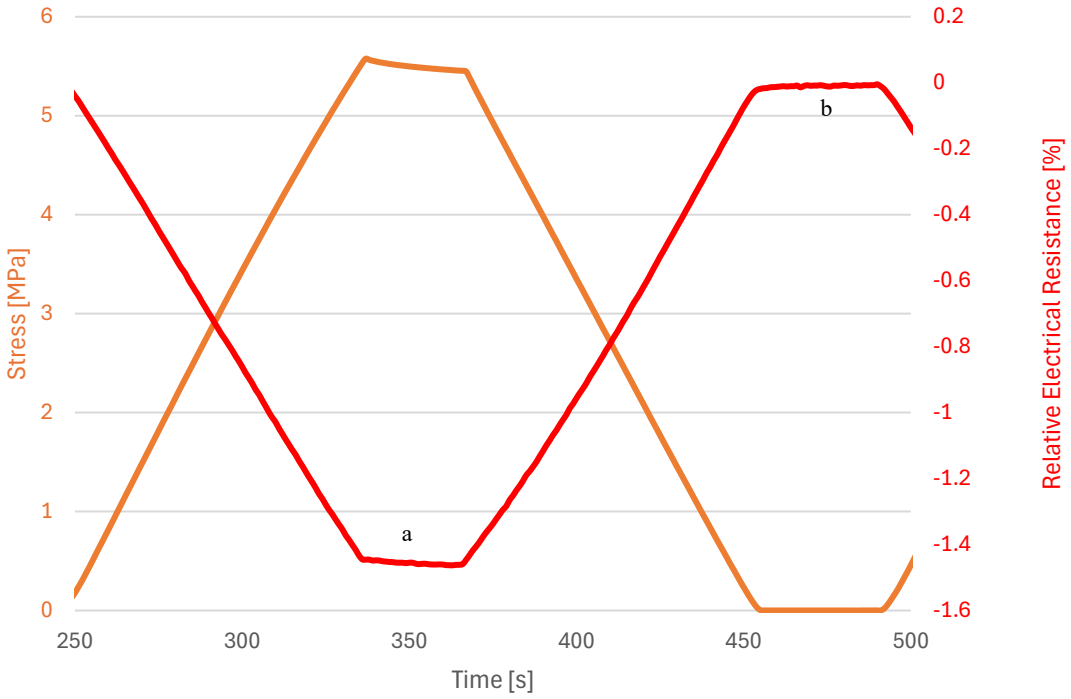

Figure 4.18 – Detail for second cycle from the representative cyclic strain and relative electrical resistance in function of time for auxetic topology with dwell.

For the sake of future reference, some values are compiled bellow for both the static and cyclic tests (Table 4.3), and cyclic tests with dwell (Table 4.4) for the auxetic structure topology.

Table 4.3 – Summary of data collected from the three-point bending static and cyclic testing for auxetic topology.

Tests	Values	Mean	Std.Dev.
Static testing	Max. Stress [MPa]	7.2	0.21
	Elastic Modulus [MPa]	39.5	4.9
	Absorbed Energy [J/mm3]	0.15	0.01
1st cycle	Max. Stress [MPa]	6.9	0.24
	Elastic Modulus [MPa]	59.50	1.1
5th cycle	Max. Stress [MPa]	6.66	0.24
	Elastic Modulus [MPa]	50.35	2.0
10th cycle	Max. Stress [MPa]	6.57	0.24
	Elastic Modulus [MPa]	48.47	1.8

Table 4.4 – Summary of data collected from the representative cyclic testing with dwell for auxetic topology.

Dwells	Values	
1st dwell	Initial Stress [MPa]	5.7
	Final Stress [MPa]	5.5
	Initial Elastic Modulus [MPa]	44.5
	Final Elastic Modulus [MPa]	43.2
5th dwell	Initial Stress [MPa]	5.4
	Final Stress [MPa]	5.3
	Initial Elastic Modulus [MPa]	42.4
	Final Elastic Modulus [MPa]	41.7
10th dwell	Initial Stress [MPa]	5.3
	Final Stress [MPa]	5.2
	Initial Elastic Modulus [MPa]	41.6
	Final Elastic Modulus [MPa]	40.9

4.1.3. Cubic

Finally, the cubic topology is represented by a graph obtained from a representative test, as was done before (Figure 4.19).

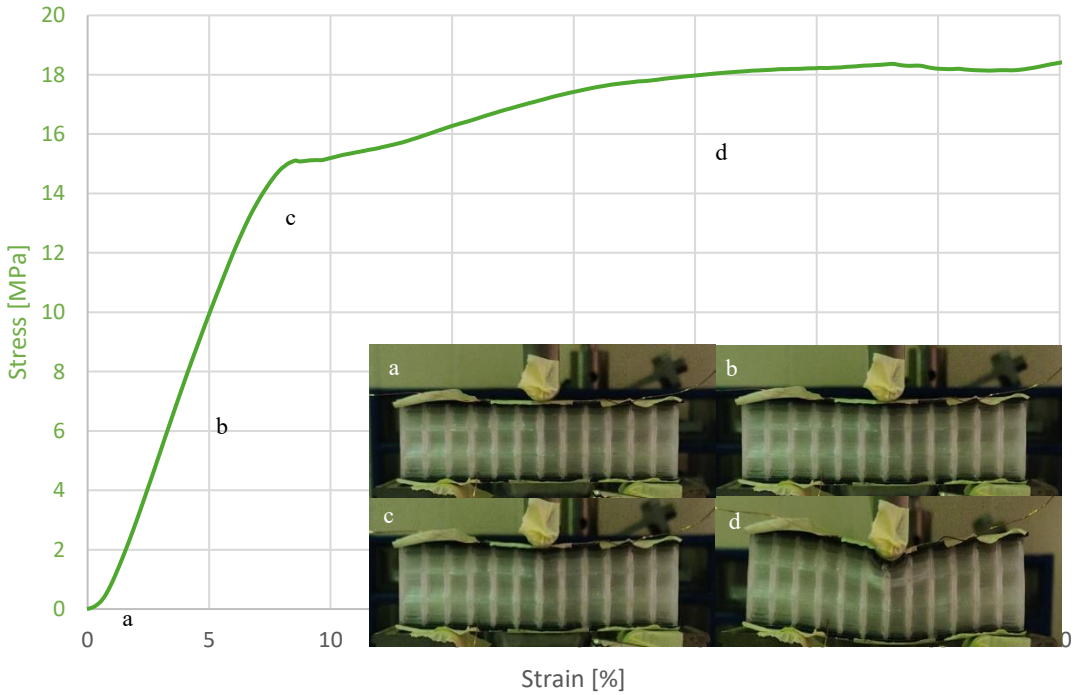

Figure 4.19 – Evolution of representative static stress versus strain graph for cubic structure topology with corresponding photographs of different test moments.

The phase of initial adjustment is rather pronounced for the cubic topology (a), ending at around 0.44 % strain (0.18 MPa stress). The samples show no visual deformation yet.

Elastic behaviour then lasts until around 7 % strain (13.8 MPa stress), with a linear curve as indicated by Hooke's Law (b). At this point, the samples seem mostly unaltered, however some

deformation can be seen by looking closely at the cells, particularly at their horizontal walls. The 8.40 % strain (15.0 MPa) point marks a local point of maximum stress (c). The top skin has begun to deform visually at this point, and the cells, particularly those in the centre two to four columns, have continued to deform. Unlike the previous topologies, there is no appreciable decrease in stress during the initial plastic behaviour, and the graph increases in stress immediately and continuously from the previous point until 40 % strain (d). By then, the two centre cells of the top layer have buckled entirely, and so the upper skin has become very deformed. Notably, the lower skin has suffered minimal deformation.

A new version of the graph, with no photos, allows for a better visualisation of the area under the curve of the graph (Figure 4.20).

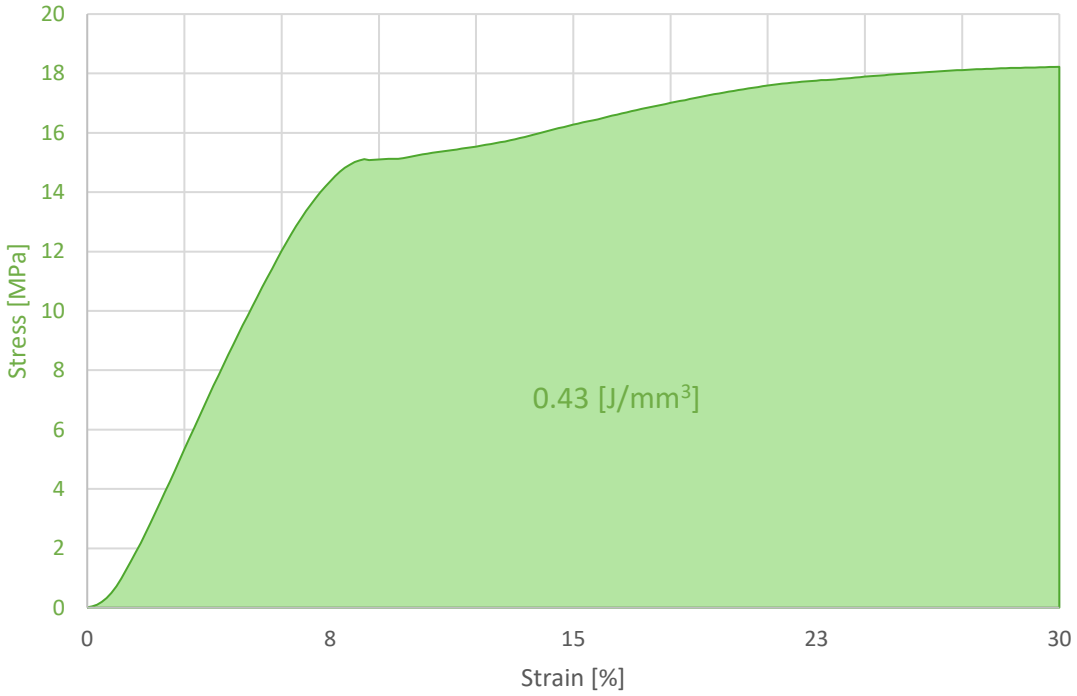

Figure 4.20 – Representative three-point bending stress versus strain graph up to 30 % strain and corresponding storage of energy for cubic topology.

Up to the 30 % strain, the absorbed energy for the elastic phase and part of the plastic phase can be obtained for the cubic topology: an estimated 0.43 J/mm^3; this value is significantly greater than that seen in the other structural geometries.

Again, a stress and relative electrical resistance versus displacement graph is plotted, to examine the electrical response (Figure 4.21).

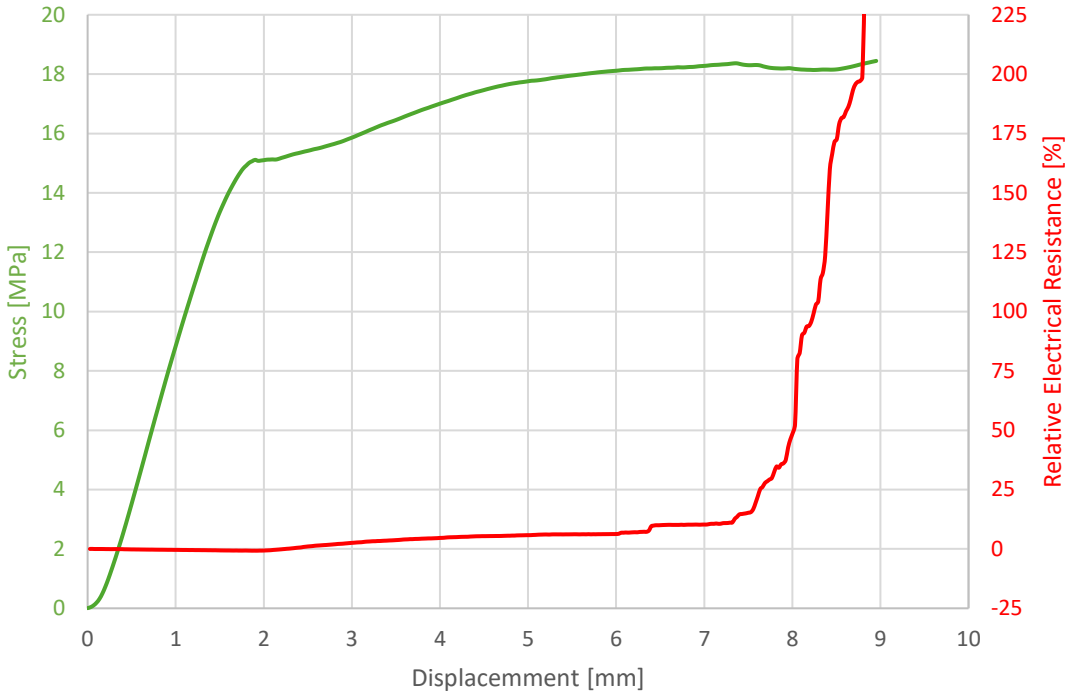

Figure 4.21 – Representative three-point bending stress versus displacement up to 10 mm and corresponding relative electrical resistance for auxetic topology.

As with the other structural geometries, the curves before the first inflection point for the stress (which corresponds to a point of maximum stress) are largely linear. However, after that point, there seems to be little change in behaviour for the relative electrical resistance. At around the 7.5 mm of displacement, the relative electrical resistance increases dramatically and continues to do so until just before the 9 mm of displacement, where it momentarily reaches a value of around $3x10^{34}$ %, then drops back to a value closer to those found during the rest of the tests, at -10 %. The most likely explanation for this is that the region of the upper skin between the electrodes reached a damage threshold, resulting in an extreme degree of electrical resistance.

To properly assess the graphs and determine whether the relative electrical resistance displays an inflection point at the maximum stress, a closer look is needed (Figure 4.22).

In this view, the progression for the relative electrical resistance is clearer, and an inversion can be seen in the 1.8 to 2 mm displacement bracket. The same can be said for the stress curve, though short-lived in comparison, since the stress then continues to increase at a lower rate, to a plateau further down the test.

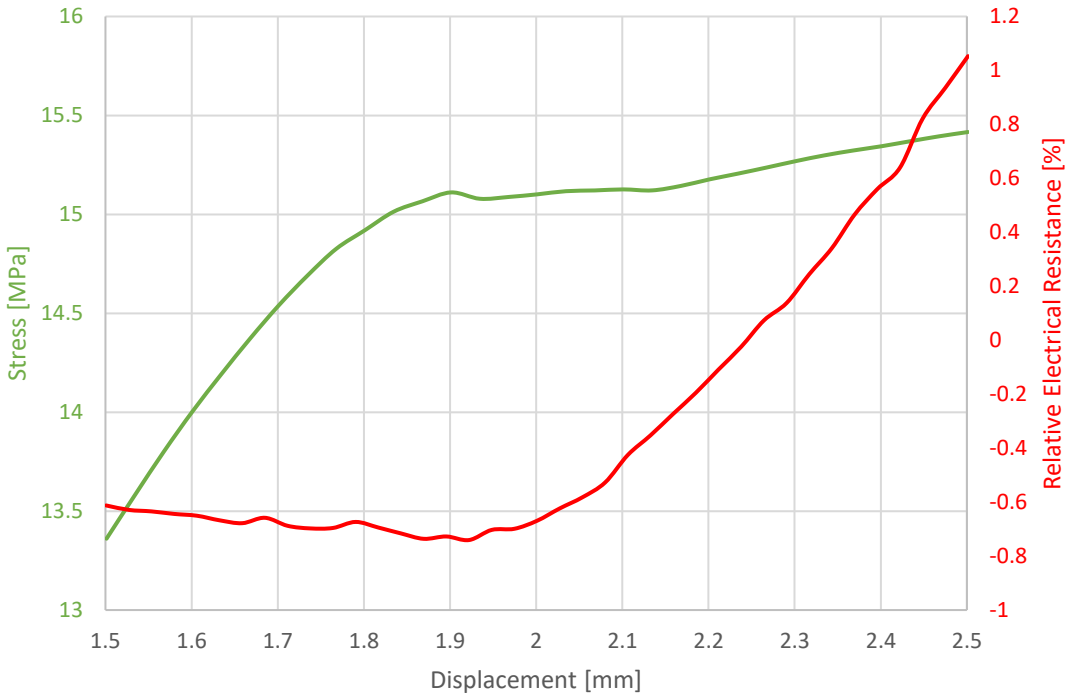

Figure 4.22 – Detail for the 1.5 to 2.5 mm interval of the three-point bending stress versus displacement graph and corresponding relative electrical resistance for cubic topology.

Proceeding now with the cyclic testing for the elastic behaviour and electrical response of the cubic topology, the following graphs were obtained (Figure 4.23).

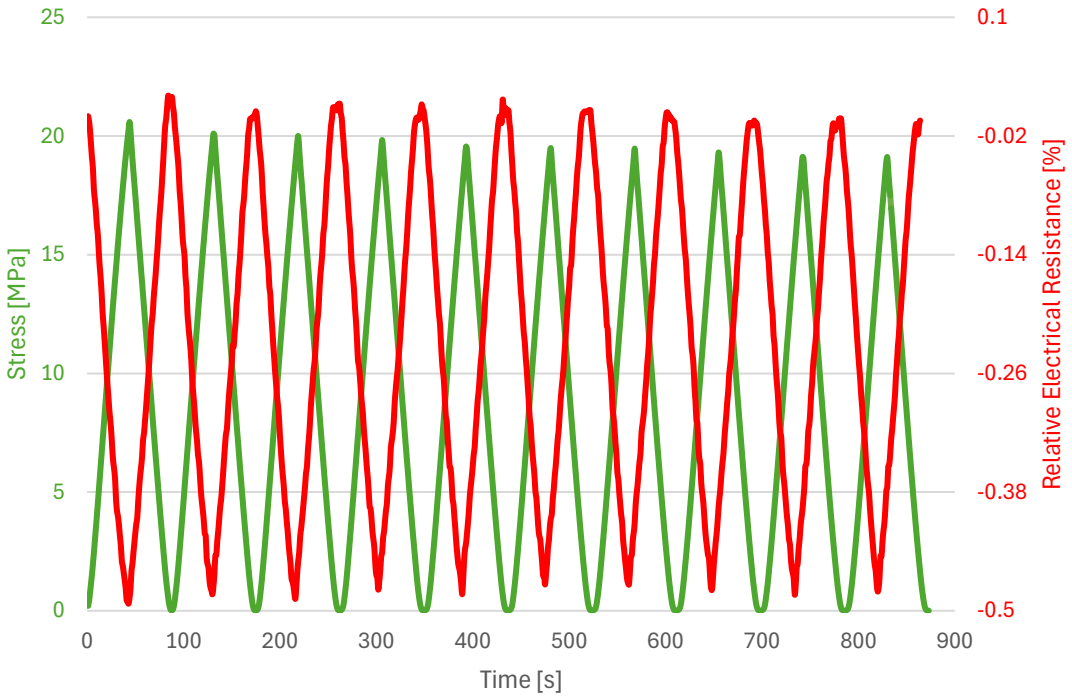

Figure 4.23 – Representative cyclic stress and relative electrical resistance in function of the time for cubic topology.

As before, the changes in the strain – increasing and decreasing cyclically in a consistent manner – are met with a directly proportional stress curve and an inversely proportional relative electrical resistance curve, i.e. the sample presents negative piezoresistivity (as was observed for the other structural geometries). And again, the maximum stress and displays a tendency to decrease with each cycle. In the case of the relative electrical resistance, there is considerable noise for the maximum values; while this is not indicative of the electrical response overall, since it is present between cycles, where an accidental release of the sample is likely, it hampers observations on its evolution throughout the test. The minimum relative electrical resistance also seems to not display a tendency overall, varying with each cycle erratically. Between the first and second cycles, the maximum stress decreases 2.4 %; while the maximum relative electrical resistance decreases 6.6 %, and the minimum increases 1.9 %. These inconsistencies may be considered inconsequential, since the cyclic range for the relative electrical resistance remains a 0.5 % for the first, fifth and tenth cycles, which suggests some constancy across cycles for the electrical response. Also note the growing discrepancy in the relative electrical resistance curve relative to the stress curve towards the end of the test.

From the previous graphs, a new figure can be made with a smaller time frame, for closer examination of the first and second cycles, as was done before for the other topologies (Figure 4.24).

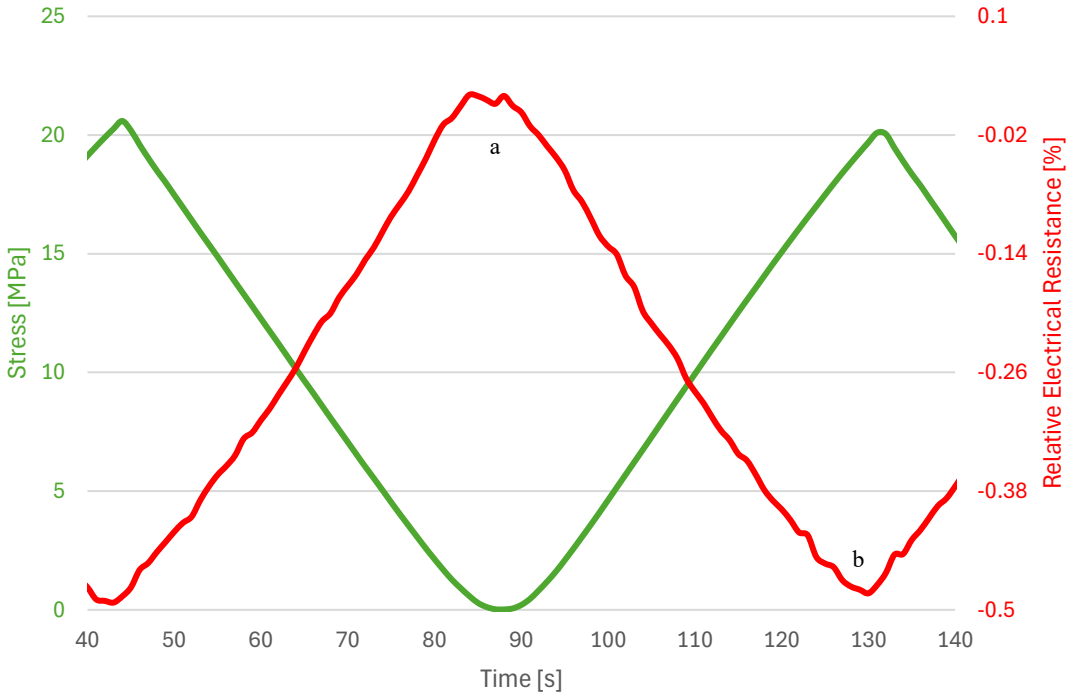

Figure 4.24 – Detail for the first and second cycles from the representative cyclic strain and relative electrical resistance in function of time for cubic topology.

In this view, the zone of the curve between cycles (a) is evidently less pronounced than the zone mid-cycle (b), even with both seeing a slight increase in noise relative to the rest of the curve. As

observed in the hexagonal and auxetic topologies, the rounder inflection points in the stress curve correspond to the rounder inflection points in the relative electrical resistance, which due to residual deformation are present between cycles.

Finishing the first set of cyclic tests, the maximum stress and gauge factor are displayed in a per-cycle basis (Figure 4.25).

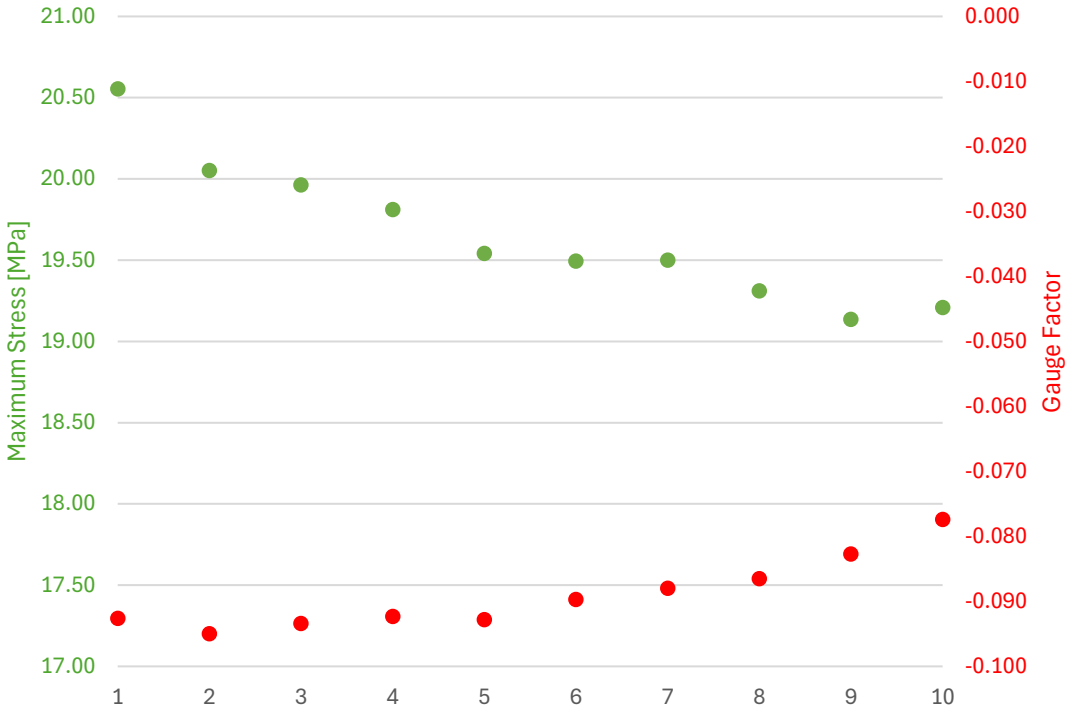

Figure 4.25 – Evolution of mean maximum stress per cycle with corresponding trend-line and gauge factor for cubic topology.

Again for the cubic topology, there is an overall reduction in the maximum stress over the course of the tests; while it starts at a 20.55 MPa, the maximum stress falls to a 93.5 % of that value by the tenth cycle. As for the gauge factor, there is no appreciable discrepancy between the value for the first cycle, and those of the other cycles. All values fit within an interval of 0.018. Despite this being a greater gap than the other geometries, it is within acceptable parameters.

After the previous stage, the cyclic tests with added dwell were carried out, resulting in the following graph (Figure 4.26).

Except for the dwells, the behaviour observed during these tests is similar to the previous cyclic tests; within the intra-cycle dwells, it is possible to observe a fall in the stress value, sharper in the first cycles and milder in the later cycles. The maximum stress consistently decreases with each cycle, while the same cannot be said of the relative electrical resistance. In fact, in some dwells the seems to be an increase in the relative electrical resistance from beginning to end, while the stress sees a decrease in value consistently.

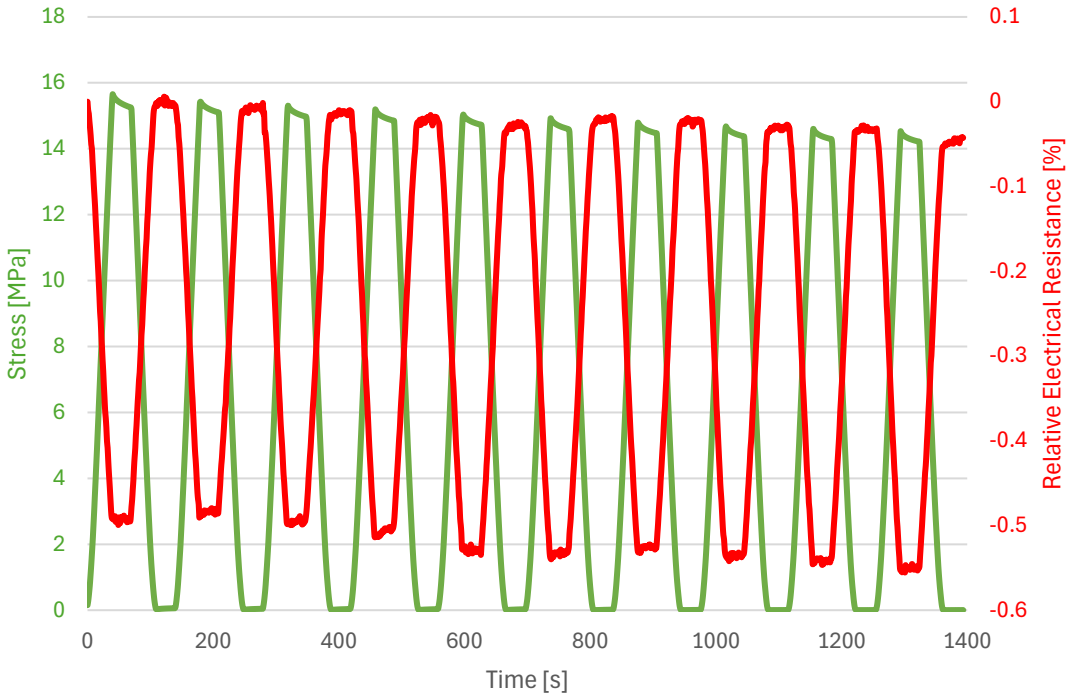

Figure 4.26 – Representative cyclic strain and relative electrical resistance in function of time for cubic topology with dwell.

As such, the same graph is observed within a narrower frame of reference (Figure 4.27).

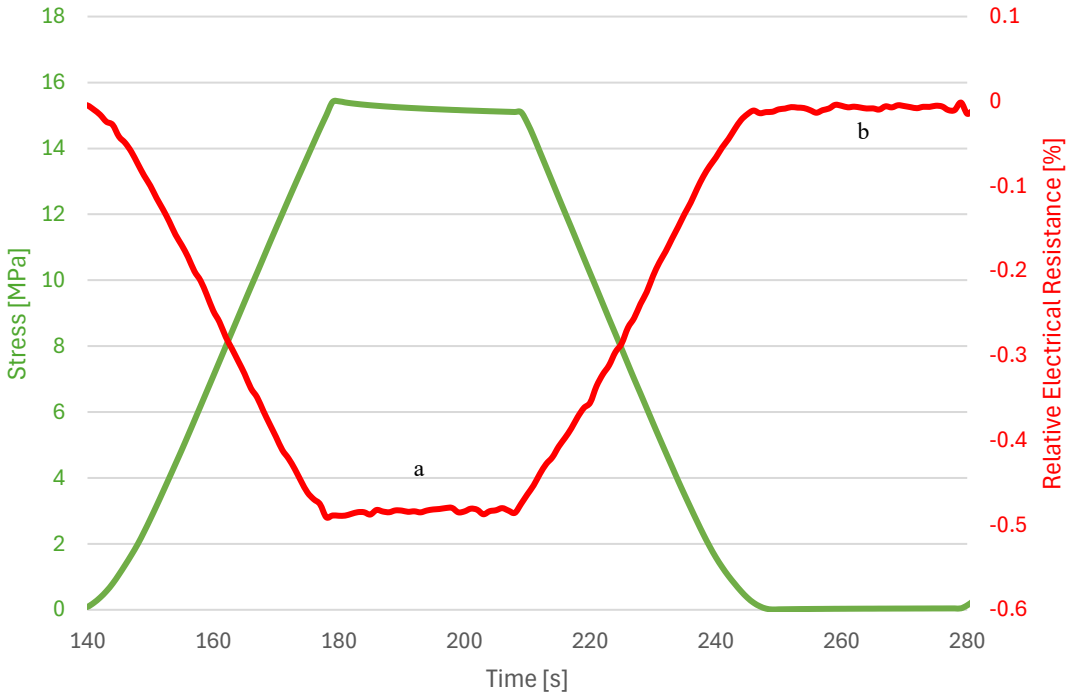

Figure 4.27 – Detail for second cycle from the representative cyclic strain and relative electrical resistance in function of time for cubic topology with dwell.

The stress curve is consistent with results from the hexagonal and auxetic topologies and shows a decrease of 2.0 % during the intra-cycle dwell (a). However, during the same period the relative electrical resistance increases a 2.9 % instead. While the stress curve is more rounded around the dwell in the inter-cycle region, this is less evident in the corresponding dwell in the relative electrical resistance curve, due to the noise in display.

For reference purposes, some values are compiled in the following tables, one for the three-point bending tests and cyclic tests (Table 4.5) and another for the cyclic tests with dwell (Table 4.6).

Table 4.5 – Summary of data collected from the three-point bending static and cyclic testing for cubic topology.

Tests	Values	Mean	Std.Dev.
Static testing	Max. Stress [MPa]	19.4	0.66
	Elastic Modulus [MPa]	236.5	21.7
	Absorbed Energy [J/mm3]	0.56	0.02
1st cycle	Max. Stress [MPa]	20.5	0.55
	Elastic Modulus [MPa]	382.7	9.9
5th cycle	Max. Stress [MPa]	19.5	0.53
	Elastic Modulus [MPa]	317.2	14.0
10th cycle	Max. Stress [MPa]	19.2	0.53
	Elastic Modulus [MPa]	294.7	13.0

Table 4.6 – Summary of data collected from the representative cyclic testing with dwell for cubic topology.

Dwells	Values	
1st dwell	Initial Stress [MPa]	15.6
	Final Stress [MPa]	15.3
	Initial Elastic Modulus [MPa]	283.9
	Final Elastic Modulus [MPa]	277.3
5th dwell	Initial Stress [MPa]	15.0
	Final Stress [MPa]	14.7
	Initial Elastic Modulus [MPa]	272.8
	Final Elastic Modulus [MPa]	267.7
10th dwell	Initial Stress [MPa]	14.5
	Final Stress [MPa]	14.2
	Initial Elastic Modulus [MPa]	263.5
	Final Elastic Modulus [MPa]	258.5

4.2 Discussion of Results

With all the tests finalised it is now possible to proceed with an overall comparison across the three structural geometries, and the discussion of the obtained results. There are certain assertions that could be made about each topology at first sight, however it would be best to quantify the difference between each of them. To that end, the relevant information from each topology is combined into three tables (Table 4.7, Table 4.8, and Table 4.9).

Table 4.7 – Summary of data collected from the three-point bending tests for hexagonal, auxetic and cubic topologies.

	Structural geometries					
	Hexagonal		Auxetic		Cubic	
Values	Mean	Std.Dev.	Mean	Std.Dev.	Mean	Std.Dev.
Max. Stress [MPa]	7	0.6	7.2	0.21	19.4	0.66
Elastic Modulus [MPa]	72.6	3.9	39.5	4.9	236.5	21.7
Absorbed Energy [J/mm^3]	0.16	0.01	0.15	0.01	0.56	0.02

Looking at Table 4.7, the hexagonal and auxetic geometries have similar values for maximum stress, however the elastic modulus for the auxetic geometry is only 54 % that of the hexagonal one. Seeing as the energy is estimated from the area under the stress curve, and the curve for the auxetic topology drops off less than the hexagonal one after the maximum stress, the area is similar for both despite the much greater elastic modulus of the hexagonal topology. The cubic topology is the outlier of the three, with a maximum stress of 277 %, an elastic modulus of 326 %, and an absorbed energy of 350 % those of the hexagonal equivalents. The cubic topology is known for an improved energy absorption over auxetic topologies for instance, as well as increased maximum load and stiffness, as indicated by Sarvestani et al. [35].

These results are consistent with that knowledge. In fact, the greater cubic rigidity when compared to the other structures is physically self-evident and supports the reduced conformity of the cubic sample to the supports during testing when compared to the other structural geometries; this is more relevant during the cyclic tests, however.

Table 4.8 – Summary of data collected from the cyclic tests for hexagonal, auxetic and cubic topologies.

		Structural geometries					
		Hexagonal		Auxetic		Cubic	
Cycles	Values	Mean	Std.Dev.	Mean	Std.Dev.	Mean	Std.Dev.
1st cycle	Max. Stress [MPa]	8.1	0.3	6.9	0.24	20.5	0.55
	Elastic Modulus [MPa]	82.4	3.5	59.5	1.1	382.7	9.9
5th cycle	Max. Stress [MPa]	7.7	0.3	6.7	0.24	19.5	0.53
	Elastic Modulus [MPa]	78.6	3.3	50.4	2	317.2	14
10th cycle	Max. Stress [MPa]	7.6	0.3	6.57	0.24	19.2	0.53
	Elastic Modulus [MPa]	77	3.2	48.5	1.8	294.7	13

For the cyclic tests, relations between the results across structural geometries is consistent with the previous three-point bending test results i.e. the cubic geometry has the highest values of elastic modulus and maximum stress, and the auxetic geometry the smallest values, while the hexagonal geometry sits between them both, though closer to the latter. With each progressive cycle there is a decrease in maximum stress and elastic modulus. The maximum stress sees, by the end of the tests, a decrease of 6 % for the hexagonal geometry, 5 % for the auxetic geometry, and 6 % for the cubic geometry relatively to the first cycle. This is in part due to the relaxation of the samples; Santos et al. [19] say «...this phenomenon in polymers occurs even at room temperature and at low-stress levels due to the molecular motion within the backbone polymer arrangement. This results from a combination of viscous flow and elastic deformation, due the molecular motions within the backbone polymer arrangement. » and «... molecular motions within the backbone polymer arrangement lead to the creep phenomenon that is influenced by stress levels ». Therefore, a cyclic reduction in maximum stress is expected and justified.

In the same period, the elastic modulus decreases 6 % for the hexagonal, 18 % for the auxetic, and 23 % for the cubic geometries. Note that the auxetic geometry was expected to show the least decrease in elastic modulus due to its superior elastic energy absorption relative to both the hexagonal and cubic geometries; the fact that the hexagonal geometry sees the smallest decrease by far goes against expectations.

One factor that is not conveyed by these tables is the capacity of the samples to conform to the supports, which led to a lack of linearity of the stress curves between cycles, which somewhat precludes the assessment of the mechanical / electrical response around these points, while the rest of the graph remains unaffected by that factor.

Table 4.9 – Summary of data collected from the representative cyclic tests with dwell for hexagonal, auxetic and cubic topologies.

		Structural geometries		
Dwells	Values	Hexagonal	Auxetic	Cubic
1st dwell	Initial Stress [MPa]	7.3	5.7	15.6
	Final Stress [MPa]	7.1	5.5	15.3
	Initial Elastic Modulus [MPa]	80.7	44.5	283.9
	Final Elastic Modulus [MPa]	77.7	43.2	277.3
5th dwell	Initial Stress [MPa]	6.9	5.4	15.0
	Final Stress [MPa]	6.8	5.3	14.7
	Initial Elastic Modulus [MPa]	76.2	42.4	272.8
	Final Elastic Modulus [MPa]	74.4	41.7	267.7
10th dwell	Initial Stress [MPa]	6.8	5.3	14.5
	Final Stress [MPa]	6.6	5.2	14.2
	Initial Elastic Modulus [MPa]	74.5	41.6	263.5
	Final Elastic Modulus [MPa]	72.9	40.9	258.5

Outside of the dwell period, the evolution of the maximum stress and elastic modulus is similar to the standard cyclic tests, with both values decreasing with the ongoing cycles. The same decline is also present within the dwells; in the first dwell, both the final stress and the final elastic modulus are 3.8 %, 3.0 % and 2.3 % lower than initially for the hexagonal, auxetic and cubic topologies respectively. During the fifth dwell both the stress and elastic modulus suffer a reduction of 2.3 %, 1.8 % and 1.9 % for hexagonal, auxetic and cubic topologies respectively. In the tenth dwell, from beginning to end, the stress and elastic modulus lower a 2.1 % / 1.7 % / 1.9 % for the hexagonal / auxetic / cubic geometries. This reduction is also supported by the same factors that cause the cyclic reduction of the maximum stress, as was described in the previous cyclic tests section.

Additionally, note the inconsistent evolution of the relative elastic resistance for the cubic geometry, compared to the others; while hexagonal and auxetic topologies show consistent reductions during dwells, the cubic topology does not. However, also note that the values for the relative elastic resistance are significantly lower for the cubic geometry; it is therefore possible that these evolutions could not be measured accurately by the equipment employed. Since both the cyclic relative electrical resistance's range and gauge factor during the standard cyclic cubic tests (Figure 4.23 / Figure 4.25) indicate good quality for electrical response, that incongruence can be considered inconsequential.

5. Conclusion

With the analysis of the obtained data concluded, it is possible to now proceed with the closure of this work, evaluating whether the objectives that were set out initially were reached and what significant meaning can be gleaned from the observations made throughout, as well as what further research possibilities are available.

5.1 Overview

As previously described in Chapter 3, the samples were designed, produced, tested and evaluated in accordance with established procedures; out of the complete process, the production and evaluation phases were particularly enriching through unexpected hurdles and findings.

Regarding the development and production of the samples the fabrication of both the skins and the cores was ultimately successful, albeit not without setbacks. The mating of both components was also resolved and, at this point in time after the tests, has not experienced any failures. Moreover, the inverse piezoresistive effect was observed for all the geometries and was shown, through the gauge factor, to be sufficiently accurate therefore proving the multifunctional capabilities of the samples and confirming the viability of its inclusion for those types of structure.

As for the mechanical behaviour, certain particularities were observed when comparing the different cores: for example, in the initial three-point bending tests, the cubic geometry stood out with a maximum stress of 19.4 MPa, which is 277 % of the value observed for the hexagonal geometry and 269 % of that for the auxetic geometry; an elastic modulus of 236.5 MPa, which is 325 % and 598 % of that for the hexagonal and auxetic geometries respectively; and an estimated energy absorbed of 0.56 J/mm^3, which is equivalent to 350 % of that for the hexagonal samples and 373 % of that for the auxetic ones. Another outlier was the maximum strain achieved by the auxetic geometry at the yield point, 25.6%, which is 175% of the strain of the hexagonal geometry; which has a yield point with a strain of 14.6%, and 296% of the strain of the cubic geometry (which reached a strain of 8.63%).

However, the cyclic tests highlighted the cyclic evolution of maximum stress and elastic modulus, wherein the hexagonal geometry was shown to suffer the least reduction in elastic modulus of all the topologies, decreasing by 6 % over ten cycles, while the decrease observed for the auxetic geometry was 300 % of this (i.e. a total of 18 %) and the cubic geometry was 383 % of the hexagonal equivalent (i.e. a total of 23 %). The cyclic evolution of maximum stress was largely consistent across the geometries, as was the evolution of both maximum stress and elastic modulus during the dwell periods. The fact that the hexagonal geometry, rather than the auxetic geometry, displayed the smallest cyclic decrease to the elastic modulus – unlike what is suggested in current literature, which emphasises auxetic metastructures as possessing superior fatigue properties over conventional structures [36] – may be due to the fact that the auxetic cells deformed poorly during testing due to improper alignment of the cells relative to the direction of deformation. However, the orientation of the auxetic cells – as well as that of the hexagonal geometry – follows the choices made in the reviewed literature where comparisons between these

geometries were present. This matter was not considered to be within the scope of this work and was therefore not explored experimentally.

Essentially, it can be concluded that the cores with a cubic cell geometry demonstrated greater stiffness, while the auxetic cell geometries displayed a capacity to reach greater strains before yielding, and the hexagonal geometries showed the smallest decline in elastic modulus and stress on a cycle-by-cycle basis of all three geometries.

Notably perhaps, the junction of a cubic-cell sandwich composite with a piezoresistive component offers new insights into the effects that the use of three-dimensional cells – uniquely granted by additive manufacturing techniques – have in the electrical behaviour of piezoresistive capabilities, in particular in contrast with other geometries, such as the hexagonal topologies which are currently industrially prevalent.

Moreover, these alternatives to traditional core geometries demonstrated mechanical benefits over the traditional hexagonal cell configuration that suggest a significant potential for practical applications in the aerospace sector. For instance, the capacity for enduring a greater strain before yield or catastrophic failure makes auxetic-celled cores a suitable alternative for wing components. The auxetic cores also demonstrated greater flexibility than the cubic cores, which is crucial for an aircraft wing. The cubic cores, although more rigid than their auxetic counterparts, and more prone to structural failure under minimal deformation, reached a much greater maximum stress during testing and could absorb much more energy, making them more suitable for structural components where their lack of flexibility is not a disadvantage, such as tail and fuselage structures. In fact, their use in a fuselage structure should be especially advantageous over other cores due to their greater stress, possibly freeing up more internal space than a mechanically equivalent hexagonal/auxetic structure, which is highly beneficial, especially within the fuselage, as this translates into a greater payload for nearly any given airframe.

5.2 Further research

Although the objectives set for this work have been reached, there are still avenues for further research; one such opportunity would be to attempt a greater degree of integration of the components that make up the sandwich, which can be achieved by building whole samples via additive manufacturing for instance. However, the production of an entire sample with the degree of multifunctionality of those found in this work in one single printing process presents a significant challenge: however, printers prepared for the simultaneous use of multiple materials are readily available, and the introduction of piezoresistive capacity into one of the materials is already possible with some newer commercially available filaments. Alternatively, another potential milestone would be to create a new filament with piezoresistive capabilities, specifically optimised for a particular type of printing.

Another option would be to create samples with improved mechanical characteristics by adding new elements to them; for example, filling the open space within the core cells with a foam could improve the thermal insulation properties of the samples. A machine capable of printing a part while also filling and setting the foam before sealing the cells could result in a fully automated process, however this would require the development of novel equipment.

There are also a number of other possibilities not as closely related, but still relevant: repeating these tests for other new cell geometries; realising different kinds of tests on the same type of samples created for this work (e.g. long-term cyclic tests to test fatigue and creep, tests at different temperatures and/or pressures to simulate diverse atmospheric conditions, etc.); or even the development of computer-aided simulations as a digital twin to the procedures found in this work, to name just a few.

References

[1] C. M. Ezhilarasu, Z. Skaf, and I. K. Jennions, 'The application of reasoning to aerospace Integrated Vehicle Health Management (IVHM): Challenges and opportunities', *Progress in Aerospace Sciences*, vol. 105, pp. 60–73, Feb. 2019, doi: 10.1016/J.PAEROSCI.2019.01.001.

[2] N. N. Sousa, P. V. Gamboa, A. M. P. Silva, and J. P. N. Pereira, 'Sandwich for aeronautical applications: mechanical and electrical characterization', Dissertação de Mestrado em Engenharia Aeronáutica, Universidade da beira Interior, 2018, http://hdl.handle.net/10400.6/8739.

[3] B. Castanie, C. Bouvet, and M. Ginot, 'Review of composite sandwich structure in aeronautic applications', *Composites Part C: Open Access*, vol. 1, p. 100004, Aug. 2020, doi: 10.1016/J.JCOMC.2020.100004.

[4] A. Fink and C. Einzmann, 'Discrete tailored asymmetric sandwich structures', *Compos Struct*, vol. 238, p. 111990, Apr. 2020, doi: 10.1016/J.COMPSTRUCT.2020.111990.

[5] V. Birman and G. A. Kardomateas, 'Review of current trends in research and applications of sandwich structures', *Compos B Eng*, vol. 142, pp. 221–240, Jun. 2018, doi: 10.1016/J.COMPOSITESB.2018.01.027.

[6] W. Yuan, H. Song, and C. Huang, 'Failure maps and optimal design of metallic sandwich panels with truss cores subjected to thermal loading', *Int J Mech Sci*, vol. 115–116, pp. 56–67, Sep. 2016, doi: 10.1016/J.IJMECSCI.2016.06.006.

[7] X. G. Zhang, X. Ren, W. Jiang, X. Y. Zhang, C. Luo, Y. Zhang, and Y. M. Xie, 'A novel auxetic chiral lattice composite: Experimental and numerical study', *Compos Struct*, vol. 282, p. 115043, Feb. 2022, doi: 10.1016/J.COMPSTRUCT.2021.115043.

[8] A. Ingrole, A. Hao, and R. Liang, 'Design and modeling of auxetic and hybrid honeycomb structures for in-plane property enhancement', *Mater Des*, vol. 117, pp. 72–83, Mar. 2017, doi: 10.1016/J.MATDES.2016.12.067.

[9] W. Wu, D. Qi, H. Liao, G. Qian, L. Geng, Y. Niu, and J. Liang, 'Deformation mechanism of innovative 3D chiral metamaterials', *Sci Rep*, vol. 8, no. 1, p. 12575, 2018, doi: 10.1038/s41598-018-30737-7.

[10] K. Li, Y. Zhang, Y. Hou, L. Su, G. Zeng, and X. Xu, 'Mechanical properties of re-entrant anti-chiral auxetic metamaterial under the in-plane compression', *Thin-Walled Structures*, vol. 184, p. 110465, Mar. 2023, doi: 10.1016/J.TWS.2022.110465.

[11] X. Wang, M. Jiang, Z. Zhou, J. Gou, and D. Hui, '3D printing of polymer matrix composites: A review and prospective', Feb. 01, 2017, *Elsevier Ltd*. doi: 10.1016/j.compositesb.2016.11.034.

[12] A. N. Dickson, J. N. Barry, K. A. McDonnell, and D. P. Dowling, 'Fabrication of continuous carbon, glass and Kevlar fibre reinforced polymer composites using additive manufacturing', *Addit Manuf*, vol. 16, pp. 146–152, Aug. 2017, doi: 10.1016/j.addma.2017.06.004.

[13] N. van de Werken, H. Tekinalp, P. Khanbolouki, S. Ozcan, A. Williams, and M. Tehrani, 'Additively manufactured carbon fiber-reinforced composites: State of the art and perspective', Jan. 01, 2020, *Elsevier B.V.* doi: 10.1016/j.addma.2019.100962.

[14] A. Roschli, K. T. Gaul, A. M. Boulger, B. K. Post, P. C. Chesser, L. J. Love, F. Blue, and M. Borish, 'Designing for Big Area Additive Manufacturing', *Addit Manuf*, vol. 25, pp. 275–285, Jan. 2019, doi: 10.1016/j.addma.2018.11.006.
[15] A. D. B. L. Ferreira, P. R. O. Nóvoa, and A. T. Marques, 'Multifunctional Material Systems: A state-of-the-art review', *Compos Struct*, vol. 151, pp. 3–35, Sep. 2016, doi: 10.1016/J.COMPSTRUCT.2016.01.028.
[16] P. Matic, 'Overview of Multifunctional Materials', *Proceedings of SPIE - The International Society for Optical Engineering*, vol. 5053, Aug. 2003, doi: 10.1117/12.498546.
[17] M. Petersen, R. Bandorf, G. Bräuer, and C. P. Klages, 'Diamond-like carbon films as piezoresistors in highly sensitive force sensors', *Diam Relat Mater*, vol. 26, pp. 50–54, Jun. 2012, doi: 10.1016/J.DIAMOND.2012.04.004.
[18] N. R. Fisco and H. Adeli, 'Smart structures: Part I—Active and semi-active control', *Scientia Iranica*, vol. 18, no. 3, pp. 275–284, Jun. 2011, doi: 10.1016/J.SCIENT.2011.05.034.
[19] B. V. Santos, A. M. P. Silva, and J. P. N. Pereira, 'Piezoresistive Sensing for Structural Health Monitoring: A Practical Application in Adhesive Joints', Dissertação de Mestrado em Engenharia Aeronáutica, Universidade da beira Interior, 2024, http://hdl.handle.net/10400.6/14836.
[20] C. Yan, P. Guo, J. Zhou, R. Chen, and A. Wang, 'Dependence of piezoresistive behavior upon Cu content in Cu-DLC nanocomposite films', *Diam Relat Mater*, vol. 136, p. 109935, Jun. 2023, doi: 10.1016/J.DIAMOND.2023.109935.
[21] M. Debiasi, H. Khoo, Y. Bouremel, S. c Luo, and E. Zhiwei, *Shape Change of the Upper Surface of an Airfoil by Macro Fiber Composite Actuators*. 2011. doi: 10.2514/6.2011-3809.
[22] M. Lin and F. K. Chang, 'The manufacture of composite structures with a built-in network of piezoceramics', *Compos Sci Technol*, vol. 62, no. 7–8, pp. 919–939, Jun. 2002, doi: 10.1016/S0266-3538(02)00007-6.
[23] Y. Wang and D. Inman, 'Simultaneous Energy Harvesting and Gust Alleviation for a Multifunctional Wing Spar Using Reduced Energy Control Laws via Piezoceramics', *J Compos Mater*, vol. 47, pp. 125–146, Jan. 2013, doi: 10.1177/0021998312448677.
[24] A. Y. N. Sofla, S. A. Meguid, K. T. Tan, and W. K. Yeo, 'Shape morphing of aircraft wing: Status and challenges', *Mater Des*, vol. 31, no. 3, pp. 1284–1292, Mar. 2010, doi: 10.1016/J.MATDES.2009.09.011.
[25] S. Oehler, D. Hartl, R. Lopez, R. Malak, and D. Lagoudas, 'Design optimization and uncertainty analysis of SMA morphing structures', *Smart Materials & Structures - SMART MATER STRUCT*, vol. 21, Sep. 2012, doi: 10.1088/0964-1726/21/9/094016.
[26] W. M. Huang, Z. Ding, C. C. Wang, J. Wei, Y. Zhao, and H. Purnawali, 'Shape memory materials', *Materials Today*, vol. 13, no. 7–8, pp. 54–61, Jul. 2010, doi: 10.1016/S1369-7021(10)70128-0.
[27] P. Keller, M. Lake, D. Codell, R. Barrett, R. Taylor, and M. Schultz, *Development of Elastic Memory Composite Stiffeners for a Flexible Precision Reflector*. 2006. doi: 10.2514/6.2006-2179.
[28] 'TDS (Technical DataSheets)'. Accessed: Feb. 28, 2025. [Online]. Available: https://www.esun3d.com/zldownload_catalog/tds/
[29] B. T. Fernandes, T. A. Dutra, A. M. P. Silva, and M. L. Aguiar, '3D Printed PETG S-Shaped Auxetic Structure: An Experimental and Numerical Study',

Dissertação de Mestrado em Engenharia Aeronáutica, Universidade da beira Interior, 2024, http://hdl.handle.net/10400.6/14850.
[30] 'Sicomin SR8100'. Accessed: Feb. 28, 2025. [Online]. Available: https://www.timeout.de/sicomin-sr8100-epoxidharz-5-78-kg-injektionsharz
[31] 'Sicomin SD8824', Accessed: Feb. 28, 2025. [Online]. Available: https://www.timeout.de/sicomin-sd8824-standardhaerter-1-28-kg-haerter-fuer-injektionsharze-sr8100
[32] A. International and files indexed by mero, 'Standard Test Methods for Flexural Properties of Unreinforced and Reinforced Plastics and Electrical Insulating Materials 1'.
[33] R. G. Ferreira, A. P. Silva, and J. Nunes-Pereira, 'Current On-Skin Flexible Sensors, Materials, Manufacturing Approaches, and Study Trends for Health Monitoring: A Review', *ACS Sens*, vol. 9, no. 3, pp. 1104–1133, Mar. 2024, doi: 10.1021/acssensors.3c02555.
[34] R. Lima, P. Costa, J. Nunes-Pereira, A. P. Silva, C. R. Tubio, and S. Lanceros-Mendez, 'Additive manufacturing of multifunctional epoxy adhesives with self-sensing piezoresistive and thermoresistive capabilities', *Compos B Eng*, vol. 293, p. 112130, Mar. 2025, doi: 10.1016/J.COMPOSITESB.2025.112130.
[35] H. Yazdani Sarvestani, A. H. Akbarzadeh, A. Mirbolghasemi, and K. Hermenean, '3D printed meta-sandwich structures: Failure mechanism, energy absorption and multi-hit capability', *Mater Des*, vol. 160, pp. 179–193, Dec. 2018, doi: 10.1016/J.MATDES.2018.08.061.
[36] M. Shirzad, J. Kang, G. Kim, M. Bodaghi, and S. Y. Nam, 'Bioinspired 3D-Printed Auxetic Structures with Enhanced Fatigue Behavior', *Adv Eng Mater*, Oct. 2024, doi: 10.1002/adem.202302036.